The Astrophysical Journal, 675:464–490, 2008 March 1

A *CHANDRA* STUDY OF THE ROSETTE STAR-FORMING COMPLEX. I. THE STELLAR POPULATION AND STRUCTURE OF THE YOUNG OPEN CLUSTER NGC 2244

Junfeng Wang,[1] Leisa K. Townsley,[1] Eric D. Feigelson,[1] Patrick S. Broos,[1]
Konstantin V. Getman,[1] Carlos G. Román-Zúñiga,[2,3] and Elizabeth Lada[3]
Received 2007 April 16; accepted 2007 November 8

ABSTRACT

We present the first high spatial resolution X-ray study of NGC 2244, the 2 Myr old stellar cluster in the Rosette Nebula, using *Chandra*. Over 900 X-ray sources are detected; 77% have optical or FLAMINGOS NIR stellar counterparts and are mostly previously uncataloged young cluster members. The X-ray–selected population is estimated to be nearly complete between 0.5 and 3 $M_{\odot}$. A number of further results emerge from our analysis: (1) The X-ray LF and the associated *K*-band LF indicate a normal Salpeter IMF for NGC 2244. This is inconsistent with the top-heavy IMF reported from earlier optical studies that lacked a good census of $<4\ M_{\odot}$ stars. By comparing the NGC 2244 and Orion Nebula Cluster XLFs, we estimate a total population of ~2000 stars in NGC 2244. (2) The spatial distribution of X-ray stars is strongly concentrated around the central O5 star, HD 46150. The other early O star, HD 46223, has few companions. The cluster's stellar radial density profile shows two distinctive structures: a power-law cusp around HD 46150 that extends to ~0.7 pc, surrounded by an isothermal sphere extending out to 4 pc with core radius 1.2 pc. This double structure, combined with the absence of mass segregation, indicates that this 2 Myr old cluster is not in dynamical equilibrium. (3) The fraction of X-ray–selected cluster members with *K*-band excesses caused by inner protoplanetary disks is 6%, slightly lower than the 10% disk fraction estimated from the FLAMINGOS study based on the NIR-selected sample. (4) X-ray luminosities for 24 stars earlier than B4 confirm the long-standing log $(L_X/L_{bol}) \sim -7$ relation. The Rosette OB X-ray spectra are soft and consistent with the standard model of small-scale shocks in the inner wind of a single massive star.

Subject headings: ISM: individual (Rosette Nebula) — open clusters and associations: individual (NGC 2244) — stars: formation — stars: luminosity function, mass function — stars: pre–main-sequence — X-rays: stars

Online material: color figures, machine-readable tables

1. INTRODUCTION

During their evolution from Class I protostars to zero-age main-sequence (ZAMS) stars, young stellar objects are readily identified in X-rays due to their highly elevated X-ray emission compared to the older Galactic stellar population (see reviews by Feigelson & Montmerle 1999; Favata & Micela 2003; Feigelson et al. 2007). High spatial resolution *Chandra* observations of well-known Galactic star-forming regions (e.g., the *Chandra* Orion Ultradeep Project, hereafter COUP, Getman et al. 2005b; RCW 38, Wolk et al. 2006; Cepheus B, Getman et al. 2006), more distant molecular cloud and H II region complexes (e.g., NGC 6334, Ezoe et al. 2006; NGC 6357, Wang et al. 2007; M16, Linsky et al. 2007; M17, Broos et al. 2007), the Galactic center (e.g., the Arches and Quintuplet clusters; Wang et al. 2006; Muno et al. 2006), and extragalactic star-forming regions (e.g., 30 Dor; Townsley et al. 2006a, 2006b) have greatly advanced our knowledge of star formation processes in these regions.

Moreover, these studies demonstrate the unique power of studying star formation in the X-ray band. Besides the high-energy phenomena, other new information about the young clusters such as population, membership, and star formation environs can be obtained when combining X-ray detections with knowledge obtained from longer wavelength studies. For example, although X-ray–selected samples contain a very small fraction of extragalactic sources and Galactic field stars, X-ray sources that have optical and infrared (IR) counterparts are mostly cluster members. This is in contrast to the high percentage of nonmembers in the optical/IR images where, except for those sources with massive dusty disks, membership for individual stars generally has to be ascertained via spectroscopy. In initial mass function (IMF; Kroupa 2002, 2004) studies of more distant, high-mass star-forming regions, traditional optical measurements are significantly encumbered by large reddening and membership confusion. In comparison to the massive stars, the lower mass pre–main-sequence (PMS) stellar populations are much less accessible and thus much harder to evaluate. In the past, Hα emission was used in general as a youth and membership indicator. However, in addition to the observational challenges due to prevalent bright Hα nebulosity in H II regions, the emission itself requires accretion activity in protoplanetary disks (Muzerolle et al. 1998, 2001) and thus is susceptible to the disk evolutionary stages.

It has long been recognized that X-ray emission circumvents these problems and is very effective for securing PMS membership of young clusters (Feigelson & Montmerle 1999). Modern X-ray observatories like *Chandra* and *XMM-Newton* enable identification of hundreds of individual members from their X-ray emission. In this work and subsequent papers, we report *Chandra* studies of a well-known star-forming complex, concentrating here on a new census of the low-mass cluster members and new knowledge of the IMF arising from the X-ray perspective.

The Rosette star-forming complex, situated in a large star formation site in the Perseus spiral arm, provides an ideal test bed for studying sequential formation of clusters due to the favorable

[1] Department of Astronomy and Astrophysics, Pennsylvania State University, University Park, PA 16802; jwang@astro.psu.edu.
[2] Harvard-Smithsonian Center for Astrophysics, Cambridge, MA 02138.
[3] Department of Astronomy, University of Florida, Gainesville, FL 32611.

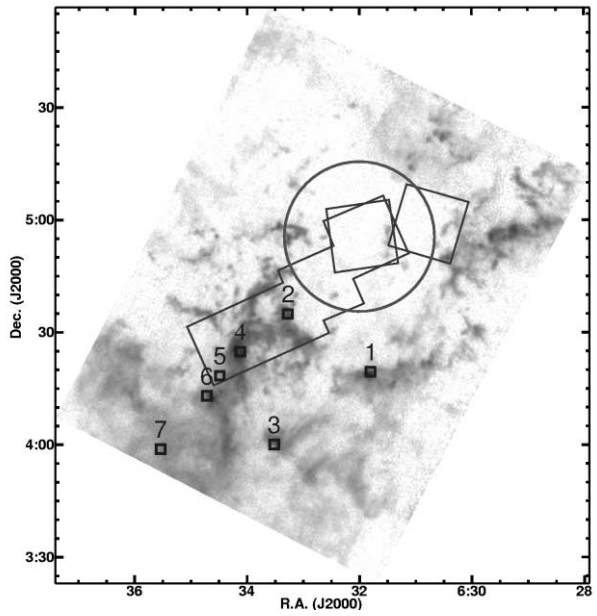

FIG. 1*a*

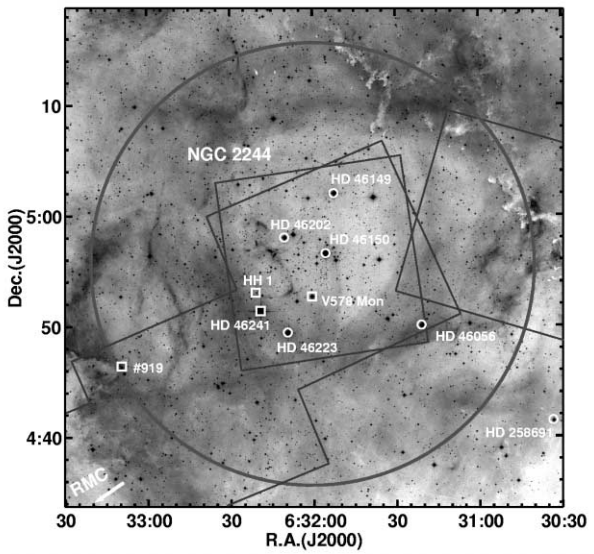

FIG. 1*b*

FIG. 1.—(*a*) Large-scale ($\sim 2^\circ \times 1.5^\circ$) view of the Rosette star-forming complex in ^{12}CO $J = 1$–0 emission from Heyer et al. (2006). The multiple ACIS FOVs (*polygons*) and the extent of the NGC 2244 cluster (*circle*) are shown. Squares mark the embedded clusters in the RMC with Phelps & Lada (1997) sequence numbers. (*b*) $45' \times 45'$ DSS2 *R*-band image of the Rosette Nebula. All known O stars in the FOV that belong to the NGC 2244 cluster (T03, Table 6) are labeled by circles. Four stars are marked as squares: V578 Mon is an eclipsing binary; HH 1 is a stellar microjet; ACIS 919 is a candidate massive star; the visually brightest star HD 46241 (K0 V) is foreground. These objects are described further in the text. [*See the electronic edition of the Journal for a color version of this figure*.]

orientation of its morphological components, consisting of an expanding blister H II region on the edge of a giant molecular cloud oriented perpendicular to the line of sight. Thorough reviews of past and present research on this popular and important star formation region appear in Townsley et al. (2003, hereafter T03) and Román-Zúñiga & Lada (2008). Here we highlight what is most relevant to this work.

The Rosette Nebula (=Sharpless 275 = W16 = NGC 2237–2239, NGC 2244, and NGC 2246) is a large H II region at the tip of the Rosette Molecular Cloud (RMC). In both radio and optical images, it shows a prominent ringlike morphology, with a cluster of ionizing young stars located in the central hole (Celnik 1985; T03). The large-scale *IRAS* data (Cox et al. 1990) and CO emission map (Heyer et al. 2006) clearly show a similar annular morphology extending into the molecular cloud (Fig. 1*a*).

Extending to the southeast of the Rosette Nebula, the RMC is an elongated giant molecular cloud with $\sim 10^5\ M_\odot$ of gas and dust (Blitz & Thaddeus 1980). Multiwavelength observations in mid-IR and radio show clumpy structure in the RMC (Williams & Blitz 1998). Embedded star clusters have been revealed in the densest parts through near-IR imaging surveys (Phelps & Lada 1997; Román-Zúñiga et al. 2005, 2008). Figure 1*a* demonstrates the association between Phelps & Lada (1997) IR clusters and the molecular clumps where the CO emission peaks. Lada & Lada (2003) have shown that embedded clusters are physically associated with the most massive and dense cores in molecular clouds, based on systematic and coordinated surveys (e.g., Lada 1992).

In the X-ray band, previous imaging study of the Rosette complex was hampered by low spatial resolution. An early *Einstein Observatory* study detected a few individual O stars and extended $\sim$2 keV X-ray emission at the center of the nebula (Leahy 1985). Berghöfer & Christian (2002) considered the integrated contribution from X-ray–emitting low-mass PMS stars in the cluster and concluded that apparently diffuse emission seen by *ROSAT* could be explained by unresolved point sources. Chen et al. (2004) analyzed the same *ROSAT* data set and attributed the brightest X-ray sources to massive stars, active T Tauri stars, and foreground stars. Gregorio-Hetem et al. (1998), studying a *ROSAT* observation of the RMC, reported faint X-ray point sources associated with T Tauri stars and Herbig Ae/Be (HAeBe) stars and X-ray "hot spots" from unresolved embedded low-mass star clusters. In T03, the first high-resolution *Chandra* X-ray image mosaic of this high-mass star-forming region was presented and soft diffuse X-ray plasma ($kT \simeq 0.06$ and $\simeq$0.8 keV) with luminosity $L_X \simeq 6 \times 10^{32}$ ergs s^{-1} was detected in the H II region. It was attributed to a combination of fast O star winds and unresolved T Tauri stars.

The young stars powering the Rosette H II region are members of the massive open cluster NGC 2244. Figure 1*b* shows a Digital Sky Survey image ($59' \times 59'$) of this region with a few bright stars and interesting objects labeled. Despite its apparent low concentration of stars in the optical, NGC 2244 contains $\sim$30 early-type stars between O4 V and B3 V (Table 6 in T03), whose cluster memberships are secured from deep photometric study along with proper-motion data and spectroscopy (Verschueren 1991; Park & Sung 2002). No other known massive young stellar cluster within 2 kpc, other than RCW 38 (Wolk et al. 2006) and M17 (Broos et al. 2007), is comparably rich. The PMS members were largely unknown from optical studies; only a handful of Hα emission objects have been identified as young PMS members (Park & Sung 2002; Li & Rector 2004). Berghöfer & Christian (2002) presented 138 sources selected from *ROSAT* PSPC and HRI detections. Although incomplete, they revealed previously unknown PMS stars to K spectral types.

The distance to NGC 2244 has been measured in many visual photometry studies and ranges between 1.4 and 1.7 kpc. Hensberge et al. (2000) derive a distance of 1.39 ± 0.1 kpc to an eclipsing binary member V578 Mon, using a novel Fourier spectral disentangling technique. The main-sequence (MS) turnoff age estimated by Park & Sung (2002) is 1.9 Myr, which is consistent

TABLE 1
Log of *Chandra* Observations

Target	ObsID	Start Time (UT)	Exposure Time (s)	Aim Point $\alpha_{J2000.0}$	Aim Point $\delta_{J2000.0}$	Roll Angle (deg)	Mode[a]
Rosette Field 1	1874	2001 Jan 05 11:53	19700	06 31 52.85	+04 55 42.0	335.86	F
Rosette Field 2	1875	2001 Jan 05 17:46	19500	06 32 40.84	+04 42 45.0	335.90	F
Rosette Field 3	1876	2001 Jan 05 23:28	19410	06 33 17.15	+04 34 42.0	335.76	F
Rosette Field 4	1877	2001 Jan 06 05:10	19510	06 34 17.34	+04 27 45.9	335.85	F
Rosette Nebula/NGC 2244	3750	2004 Jan 01 02:20	75000	06 31 56.45	+04 56 25.4	351.87	VF
NGC 2244 satellite cluster	8454	2007 Feb 09 02:25	20480	06 30 50.40	+04 59 34.0	286.00	VF

Notes.—Units of right ascension are hours, minutes, and seconds, and units of declination are degrees, arcminutes, and arcseconds. Exposure times are the net usable times after various filtering steps are applied in the data reduction process. The aim points and roll angles are obtained from the satellite aspect solution before astrometric correction is applied.

[a] The observing mode: F = Faint; VF = Very Faint.

with the inferred age from V578 Mon, 2.3 $\pm$ 0.2 Myr (Hensberge et al. 2000). This makes NGC 2244 the youngest cluster within the larger Mon OB2 association (Hensberge et al. 2000). We adopt a distance of 1.4 kpc and a cluster age for NGC 2244 of 2 Myr throughout our studies; these are consistent with T03. Note that a larger distance value $d = 1.6$ kpc has been used recently by other researchers (Park & Sung 2002; Román-Zúñiga et al. 2008). This discrepancy in distance affects our derived X-ray luminosities ($\log L_X$) by only 0.1 dex. At the distance of 1.4 kpc, $1'$ corresponds to 0.4 pc.

Whereas the T03 paper was dedicated to study of the diffuse X-ray emission in the Rosette H II region, we present here an X-ray point-source study of the Rosette complex based on T03 data and a new 75 ks *Chandra* observation centered on NGC 2244. The fields of view (FOVs) of our mosaic *Chandra* fields are outlined by the polygons in Figure 1*a*. We separate our study into a series of four papers with different astrophysical emphasis. In this work (Paper I), we report *Chandra* observations of the NGC 2244 cluster and the Rosette H II region and study the young stellar population in detail. In Paper II (J. Wang et al. 2008a, in preparation) we describe *Chandra* observations of the embedded clusters in the RMC, aiming to investigate cluster formation in a sequential manner and to test whether molecular clumps preferentially forming embedded clusters of low-mass stars make up the fundamental building blocks of star formation in molecular clouds. The westernmost *Chandra* field, designed to study triggered star formation and the X-ray detection of a twin cluster to NGC 2244 (Li 2005; Román-Zúñiga et al. 2008), will be presented in Paper III (J. Wang et al. 2008b, in preparation). A detailed analysis of the diffuse X-ray emission in the H II region will appear in Paper IV (L. Townsley et al. 2008, in preparation).

New mid-IR observations are also contributing to our knowledge of the Rosette complex. A shallow *Spitzer Space Telescope* survey of NGC 2244 has been reported (Balog et al. 2007), and a deep *Spitzer* survey for disk emission from *Chandra* stars in NGC 2244 is also underway (PI: Bouwman). Together with the *Spitzer* MIPS coverage of the massive cores in the RMC (PI: Bonnell) and a new *Spitzer* program (PI: Rieke), virtually the entire nebula and the molecular cloud will be completely mapped.

This paper is organized as follows. First, we describe the *Chandra* observations and data reduction in § 2. In § 3 we identify the X-ray sources with optical and infrared counterparts and evaluate the fraction of contaminants through simulations utilizing the stellar population synthesis model and the $\log N$–$\log S$ distribution for extragalactic X-ray sources. Section 4 is devoted to global properties of the NGC 2244 cluster such as the X-ray luminosity function (XLF), the IMF, the *K*-band luminosity function, spatial structures, mass segregation, and the *K*-band excess disk fraction among the X-ray–detected stars. We present collective properties of interesting X-ray sources in § 5, ending with a summary in § 6.

2. *CHANDRA* OBSERVATIONS AND DATA REDUCTION

The Rosette complex was observed with the Imaging Array of the *Chandra* Advanced CCD Imaging Spectrometer (ACIS-I). The ACIS-I FOV is $17' \times 17'$ in a single pointing, and a mosaic observation was designed to best image the ionizing cluster, capture the interface between the photoionized gas and the cold neutral material, step into the dense molecular cloud, and study its recently reported secondary cluster. As shown in Table 1, the entire observation consisted of four $\sim$20 ks ACIS-I snapshots in 2001 January (T03, Fig. 2), a deep 75 ks ACIS-I image in 2004 January centered on the O5 star HD 46150 in NGC 2244 (Fig. 2*a*), and one 20 ks ACIS-I pointing at the twin cluster to NGC 2244 (Li 2005) in 2007. The image mosaic covers a $\sim 1^\circ \times 0.25^\circ$ field of the Rosette Nebula and RMC. All images were taken in standard "Timed Event, Faint" mode with 3 pixel $\times$ 3 pixel event islands except ObsID 3750 and ObsID 8454, which used the "Very Faint" mode (5 pixel $\times$ 5 pixel event islands).

We follow the same customized data reduction and source extraction described in T03, Wang et al. (2007), and Broos et al. (2007). The processing of Level 1 data is presented in detail in Appendix B of T03; the same reduced data set used in that study (Rosette Fields 1–4), augmented by the deep observation (Rosette Nebula/NGC 2244) reduced following T03, was used here for further analysis. With slightly different roll angles, we reprojected the ObsID 1874 data and merged them with the ObsID 3750 field. Figure 2*a* shows the merged 94 ks ACIS image of NGC 2244 overlaid with source extraction regions (see details below). Many point sources are visible; this is further illustrated in the smoothed X-ray composite image (Fig. 2*b*) for the merged fields created with the CIAO tool `csmooth` (Ebeling et al. 2006). In Figure 2*c* the existence of soft diffuse emission is emphasized in the context of the DSS optical image, where the diffuse X-ray emission nicely fills in the cavity of the H II region. This component will be discussed in Paper IV.

2.1. *Source Finding and Photon Event Extraction*

For identifying X-ray point sources, first we assemble a large number of candidate sources using a variety of techniques and criteria, including image reconstruction and visual inspection. The source searching for NGC 2244 is performed on the merged fields from ObsID 1874 and ObsID 3750. For each of the ACIS fields,

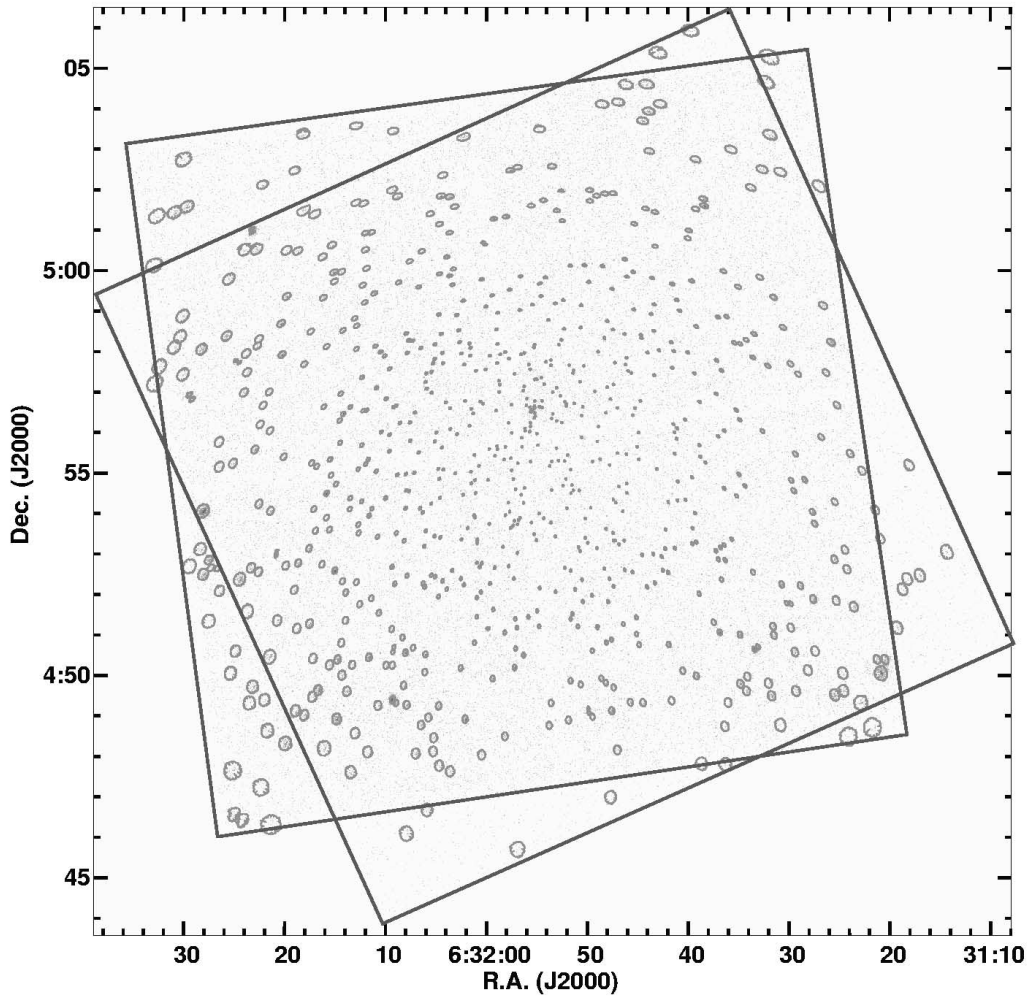

FIG. 2*a*

FIG. 2.—(*a*) Merged 94 ks ACIS-I image of the NGC 2244 cluster from ObsIDs 1874 and 3750 (outlined by two $17' \times 17'$ boxes) with reduced resolution (binned by 2 pixels). The two ObsIDs have slightly different roll angles. (*b*) X-ray composite image created from `csmooth` for the merged fields. Blue intensity is scaled to the soft (0.5–2 keV) X-ray emission, green intensity is scaled to the hard (2–7 keV) X-ray emission. (*c*) Same as (*b*), but the scaling emphasizes soft diffuse emission and red intensity is scaled to the DSS *R*-band optical emission.

12 different images were created: soft (0.5–2 keV), hard (2–7 keV), and full (0.5–7 keV) X-ray wave bands with four different pixel binning scales (4 times, ~2 times, 1 times, and 0.5 times a sky pixel). The `wavdetect` program (Freeman et al. 2002) was run with wavelet scales from 1 to 16, 8, 4, and 2 pixels in steps of $\sqrt{2}$ (for the four different binnings, respectively) and a source significance threshold of 1×10^{-5} (which is very sensitive but permits some false sources) on each of the images described above. These 12 source lists were merged, with the source position from the highest resolution image retained, to generate a single list of candidate sources.

To take advantage of the subarcsecond point-spread function (PSF) at positions around the aim point, we applied a subpixel positioning code (Mori et al. 2001) to improve spatial resolution in the inner part of the field. An image reconstruction with the Lucy-Richardson maximum likelihood algorithm (Lucy 1974) was performed in the central $50'' \times 50''$ around HD 46150 (Fig. 3) in ObsID 3750 (examples of maximum likelihood image reconstruction can be found in Townsley et al. 2006a; Wang et al. 2007). Eighteen additional candidate sources from the image reconstruction were added to the source list. Adaptive kernel smoothed flux images in the three energy bands were also created with `csmooth` to help visually identify additional faint potential sources. Source lists from all ObsIDs (except the recent observation, ObsID 8454) were then merged to form a master candidate detection list.

The source finding procedure described above results in a total of 1452 potential sources identified for five ObsIDs (omitting the westernmost field ObsID 8454). A preliminary event extraction for the potential X-ray sources was made with our customized IDL script ACIS Extract[4] (ver. 3.98, hereafter AE; Broos et al. 2002). Using the AE-calculated probability P_B that the extracted events are solely due to Poisson fluctuations in the local background, source validity can be statistically evaluated while taking into account the large distorted PSFs at far off-axis locations and spatial variations in the background. After a careful review of the net count distribution and IR counterpart frequency for all candidate sources, we rejected sources with $P_B > 0.014$, i.e., those with a 1.4% or higher likelihood of being a background fluctuation. The trimmed source list includes 1314 valid sources.

[4] Available at http://www.astro.psu.edu/xray/docs/TARA/ae_users_guide.html.

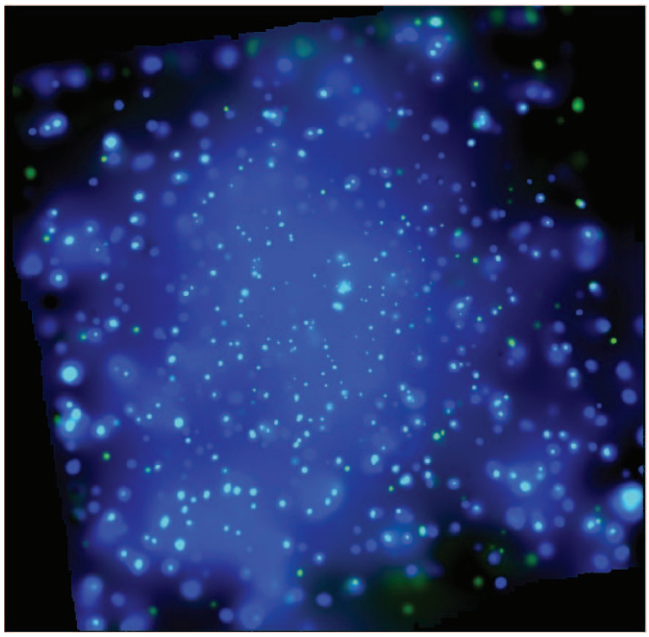

FIG. 2*b*

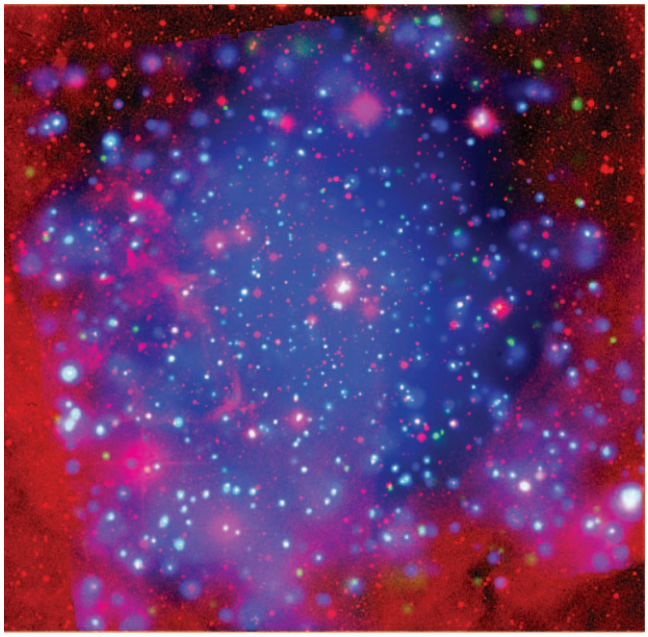

FIG. 2*c*

Since our data analysis involves multiple *Chandra* observations, for convenience and to avoid repeating source designations we divide the X-ray point sources into NGC 2244 sources and RMC sources based on positions. According to the stellar density distribution of Two Micron All Sky Survey (2MASS) sources in NGC 2244 (Li 2005), the CO emission maps (Williams et al. 1995; Heyer et al. 2006), the *IRAS* 60 μm emission (Cox et al. 1990), and radio continuum (Celnik 1985), we assign all X-ray sources within 20′ of the cluster central position (R.A. = $06^{h}31^{m}59.9^{s}$, decl. = $+04^{\circ}55'36''$) as potential NGC 2244 sources. This is indicated by the large circle in Figure 1. The resulting cluster extent is consistent with the size of this massive open cluster determined by systematic studies from the All-Sky Compiled Catalog of 2.5 Million Stars (Kharchenko et al. 2005). We remind the reader that the dividing line is not unique; ambiguity of exact physical associations certainly exists for sources located in the interface between the H II region and the molecular cloud to the east and between the main NGC 2244 cluster and secondary NGC 2237 cluster to the west. In this paper (Paper I) we focus on a total of 919 sources located within the NGC 2244 cluster region (as defined above); the rest are presented in Papers II and III.[5]

The 919 valid sources are divided into a primary list of 805 highly reliable sources ($P_B < 0.001$; Table 2) and a secondary list of 114 tentative sources with $P_B \geq 0.001$ likelihood of being spurious background fluctuations. Tables 2 and 3 have formats that are identical to Tables 1 and 2 in Townsley et al. (2006a), Wang et al. (2007), and Broos et al. (2007). A detailed description of the table columns is given in the table notes.

2.2. *Source Variability*

One of the most notable characteristics of PMS stars is flaring in the X-ray band, and a few extraordinarily powerful X-ray flares have been reported in several PMS stars (e.g., Imanishi et al. 2001; Grosso et al. 2004; Favata et al. 2005; Getman et al. 2006; Wang et al. 2007; Broos et al. 2007). A Kolmogorov-Smirnov (K-S) test is performed by AE on each observation in order to evaluate X-ray light-curve variability within that observation, comparing the source event arrival times to that of a uniform light-curve model. Seventy-eight sources display significant variability ($P_{\text{K-S}} < 0.005$ in col. [15] of Tables 2 and 3), and 14 of them have more than 200 net counts. Six of these highly variable light curves, for sources having more than 500 counts, are shown in Figure 4.

Due to the short duration (20 ks) of most of our Rosette observations, few flares are observed in their entirety. However, ObsID 3750 is 75 ks long and completely captures a giant flare from source 634 (average luminosity $\log L_{t,c} = 31.3$ ergs s^{-1}). The count rate during the flare peak is ~100 times that of the quiescent level. The estimated peak luminosity is $\log L_{t,c} = 32.3$ ergs s^{-1}. The shape of the flare is not symmetric, with a ~1.5 hr rising phase and a ~4 hr decaying phase, resembling the fast rise and slow decay X-ray flares commonly seen in the COUP young stars (Favata et al. 2005). Its IR counterpart (§ 3) does not show *K*-band excess, and the color and magnitude are consistent with a T Tauri star. The X-ray spectrum is very hard ($kT \sim 7$ keV). Multiple flares are seen in source 691 with different intensities. Source 919 is only covered in the 20 ks observation, but it shows a "flat-top" flare, characterized by a fast rise from low flux to high flux and a constant high flux level.

2.3. *Spectral Fitting*

For brighter sources with photometric significance Signif > 2.0 (col. [12] in Tables 2 and 3), the extracted spectra were fitted using single-temperature and two-temperature APEC thermal plasmas (Smith et al. 2001) and power-law models subjected to an absorbing column (N_{H}) of interstellar material with the XSPEC[6] package (ver. 12.2.1ap; Arnaud 1996), based on source spectra, background spectra, ancillary response functions (ARFs), and redistribution matrix functions (RMFs) from AE. The best-fit model was achieved by the maximum likelihood method (Cash 1979). Abundances of 0.3 $Z_{\odot}$ were assumed for the automated fitting performed by AE.

[5] A small number of sources that are in ObsID 1875 and listed in Tables 2 and 3 here will be discussed scientifically in Paper II with the RMC sources. To avoid confusion, they will not be presented in RMC source list tables, but we will list these sources separately in Paper II for consistency between the papers.

[6] See http://heasarc.gsfc.nasa.gov/docs/software/lheasoft/xanadu/xspec.

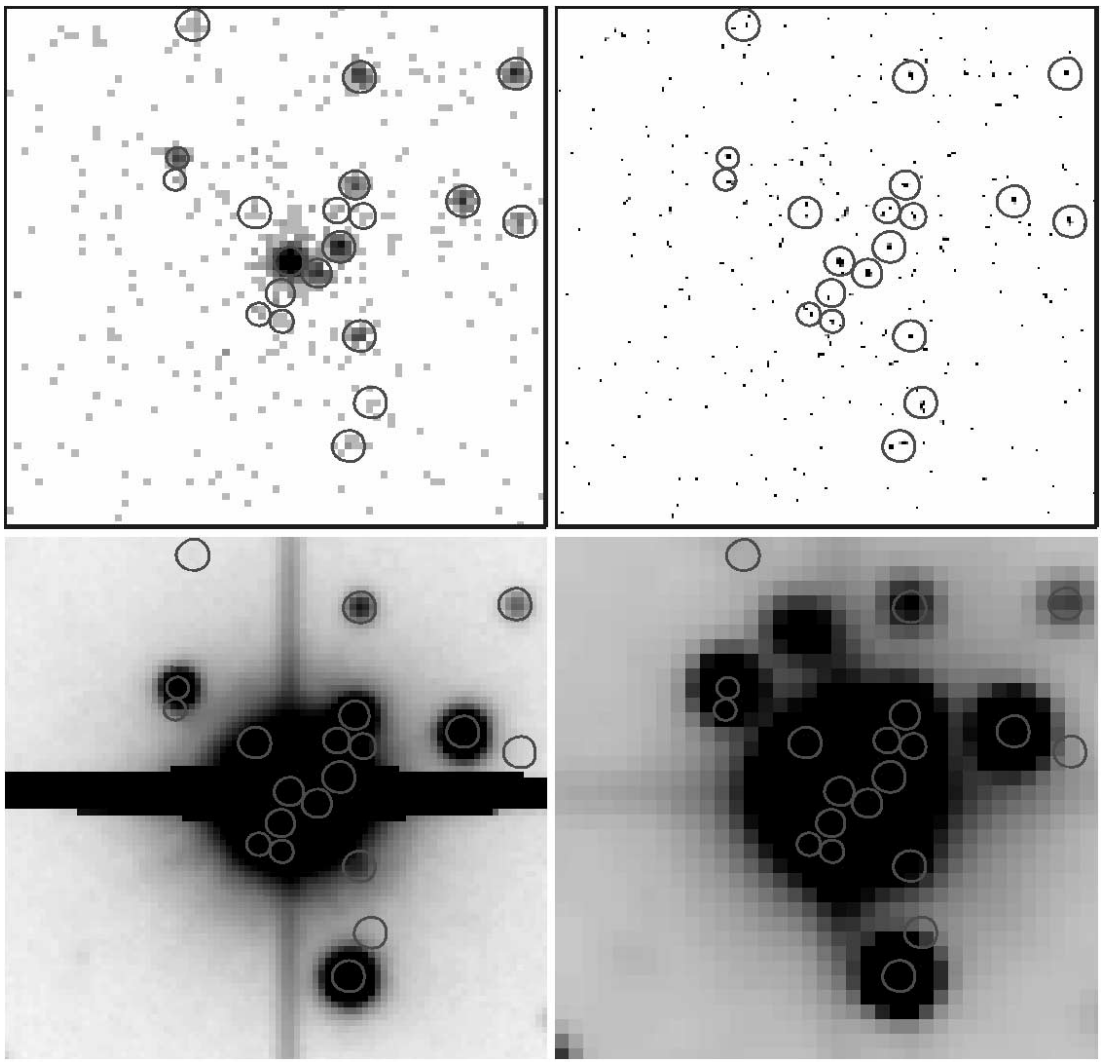

FIG. 3.—30″ × 30″ ACIS unbinned image (*top left*), reconstructed image (*top right*), Hα image (*bottom left*), and 2MASS K_s image (*bottom right*) of the central region around the O5 V star HD 46150. Several new sources are resolved within 5″ of the dominant star by the *Chandra* observation.

In general, we prefer unconstrained fits (including power-law fits) to constrained fits. The single-temperature thermal plasma APEC model is the default model used for spectral fitting. For sources brighter than 100 counts, if a one-temperature thermal plasma model did not fit the data well, a two-temperature thermal plasma model or variable abundance VAPEC thermal plasma model was invoked. A power-law model was adopted if it represented the data more adequately than the thermal model (visually or with improved statistics) or if the thermal model required nonphysical parameters (e.g., $kT \gg 15$ keV). Note that the adopted model should not be used to infer the nature of the source; a source best fitted by a power law is not necessarily an active galactic nucleus (AGN). For a number of sources that required a very hard thermal plasma and were identified with known stellar counterparts or exhibited flaring light curves that were suggestive of PMS stars, we truncated the plasma temperature at $kT = 15$ keV and adopt the thermal plasma model. When no model was acceptable, we froze the parameter $kT = 2$ keV in the thermal model, a typical value for young PMS stars (Getman et al. 2005b; Preibisch et al. 2005), and then fitted for the absorbing column density $N_{\rm H}$ and the normalization parameters. The brightest source in the field is the O star HD 46150 (ACIS 373), which has 3588 ACIS counts in 94 ks of exposure, or a count rate of 0.12 counts per CCD frame. This is not bright enough to cause multiple photon events in a single frame that would corrupt our spectral fitting; thus, it does not warrant correction for photon pileup (Townsley et al. 2002).

Spectral analysis results for the 630 sources with Signif $\gtrsim 2.0$ are presented in Table 4 (588 sources; thermal plasma fits) and Table 5 (42 sources; power-law fits). The table notes give detailed descriptions of the columns. Best-fit absorbing column densities range from negligible to $\log N_{\rm H} \sim 23.3$ cm^{-2}, equivalent to a visual absorption of $A_V \sim 120$ mag (Vuong et al. 2003). Temperatures range from $kT \sim 0.2$ keV to the hardest sources truncated at $kT = 15$ keV. The range of observed total-band (0.5–8 keV) absorption-corrected luminosities able to be derived from spectral modeling is 29.1 ergs s^{-1} $\lesssim \log L_{t,c} \lesssim$ 32.4 ergs s^{-1}. Assuming a 2 keV plasma temperature and an average $A_V = 1.5$ mag visual extinction ($\log N_{\rm H} \sim 21.4$ cm^{-2} absorbing column), PIMMS[7] gives an apparent total-band luminosity $\log L_t \sim 28.7$ ergs s^{-1} estimated for the faintest on-axis detection in Table 3. A conservative estimate for limiting sensitivity of the entire NGC 2244 observation is $\log L_t \sim 29.4$ ergs s^{-1} assuming an average extinction $A_V = 1.5$ and a 10 count detection; the exact value depends on off-axis location and absorption.

[7] The Portable, Interactive Multi-Mission Simulator is software for high-energy astrophysicists, written and maintained by Koji Mukai. See http://heasarc.gsfc.nasa.gov/docs/software/tools/pimms.html.

TABLE 2

Chandra Main Catalog: Basic Source Properties

Source		Position				Extracted Counts					Characteristics					
Seq No. (1)	CXOU J (2)	$\alpha_{J2000.0}$ (deg) (3)	$\delta_{J2000.0}$ (deg) (4)	Err (arcsec) (5)	θ (arcmin) (6)	Net Full (7)	ΔNet Full (8)	Bkgd Full (9)	Net Hard (10)	PSF Frac (11)	Signif (12)	log P_B (13)	Anom (14)	Var (15)	Eff Exp (ks) (16)	E_{median} (keV) (17)
1.....	063114.36+045303.0	97.809835	4.884189	0.9	9.9	23.3	5.7	3.7	5.8	0.91	3.7	<−5	g...	...	15.0	1.4
2.....	063117.04+045228.3	97.821033	4.874535	0.7	9.5	32.0	6.5	4.0	1.4	0.90	4.5	<−5	....	a	17.0	1.4
3.....	063118.11+045511.8	97.825464	4.919953	1.0	8.7	12.4	4.4	2.6	3.5	0.90	2.5	<−5	....	a	16.3	1.7
4.....	063118.29+045223.1	97.826245	4.873106	1.0	9.2	14.6	4.8	3.4	0.8	0.89	2.7	<−5	....	a	16.8	1.2
5.....	063118.76+045207.6	97.828205	4.868779	1.1	9.2	9.7	4.1	3.3	1.9	0.89	2.1	−4.4	....	b	17.0	1.1
8.....	063120.89+045003.8	97.837054	4.834396	0.2	10.7	599.7	25.8	33.3	32.1	0.87	22.8	<−5	....	a	81.8	1.0
311.....	063152.54+050159.1	97.968929	5.033106	0.1	5.8	299.3	17.8	0.7	0.6	0.43	16.3	<−5	....	a	85.7	0.9
373.....	063155.51+045634.2	97.981330	4.942835	0.0	0.4	3588.5	60.4	0.5	121.8	0.88	58.9	<−5	g...	...	82.6	0.9
476.....	063200.65+045241.2	98.002718	4.878124	0.1	3.8	185.9	14.2	1.1	27.3	0.89	12.6	<−5	....	a	90.6	1.2
615.....	063209.32+044924.4	98.038846	4.823469	0.1	7.7	1685.2	41.6	4.8	17.6	0.69	40.0	<−5	....	...	83.9	1.0
630.....	063210.47+045759.6	98.043639	4.966572	0.1	4.0	332.6	18.8	1.4	0.3	0.89	17.2	<−5	....	a	88.5	0.9
743.....	063220.77+045303.5	98.086542	4.884328	0.3	7.0	25.5	5.7	1.5	2.2	0.48	4.1	<−5	....	b	85.0	0.9

Notes.—The first five sources and the interesting sources shown in Fig. 1 are listed here for guidance regarding its form and content and for the convenience of the reader. Col. (1): X-ray catalog sequence number, sorted by right ascension. Col. (2): IAU designation. Cols. (3) and (4): Right ascension and declination for epoch J2000.0. Col. (5): Estimated random component of position error, 1 σ, computed as (standard deviation of PSF inside extraction region)/(number of counts extracted)$^{1/2}$. Col. (6): Off-axis angle. Cols. (7) and (8): Estimated net counts extracted in the total energy band (0.5–8 keV) and average of the upper and lower 1 σ errors on col. (7). Col. (9): Background counts extracted (total band). Col. (10): Estimated net counts extracted in the hard energy band (2–8 keV). Col. (11): Fraction of the PSF (at 1.497 keV) enclosed within the extraction region. Note that a reduced PSF fraction (significantly below 90%) may indicate that the source is in a crowded region. Col. (12): Photometric significance computed as (net counts)/(upper error on net counts). Col. (13): Log probability that extracted counts (total band) are solely from background. Some sources have P_B values above the 1% threshold that defines the catalog because local background estimates can rise during the final extraction iteration after sources are removed from the catalog. Col. (14): Source anomalies: g = fractional time that the source was on a detector (FRACEXPO from `mkarf`) is <0.9; e = source on field edge; p = source piled up; s = source on readout streak. Col. (15): Variability characterization based on K-S statistic (total band): a = no evidence for variability ($0.05 < P_{K\text{-}S}$); b = possibly variable ($0.005 < P_{K\text{-}S} < 0.05$); c = definitely variable ($P_{K\text{-}S} < 0.005$). No value is reported for sources with fewer than 4 counts or for sources in chip gaps or on field edges. Col. (16): Effective exposure time: approximate time the source would have to be observed on axis to obtain the reported number of counts. Col. (17): Background-corrected median photon energy (total band). Table 2 is published in its entirety in the electronic edition of the *Astrophysical Journal*. A portion is shown here for guidance regarding its form and content.

TABLE 3

Chandra Secondary Catalog: Tentative Source Properties

Source		Position				Extracted Counts					Characteristics					
Seq No. (1)	CXOU J (2)	$\alpha_{J2000.0}$ (deg) (3)	$\delta_{J2000.0}$ (deg) (4)	Err (arcsec) (5)	θ (arcmin) (6)	Net Full (7)	ΔNet Full (8)	Bkgd Full (9)	Net Hard (10)	PSF Frac (11)	Signif (12)	log P_B (13)	Anom (14)	Var (15)	Eff Exp (ks) (16)	E_{median} (keV) (17)
19.....	063124.47+045306.2	97.851975	4.885077	0.8	8.4	9.0	4.9	10.0	0.1	0.90	1.6	−2.1	....	a	82.8	1.5
28.....	063126.33+045728.8	97.859728	4.958023	0.8	7.4	8.0	4.4	7.0	3.0	0.90	1.6	−2.2	....	a	84.7	1.1
32.....	063127.43+045036.4	97.864312	4.843457	0.8	9.0	10.3	5.5	13.7	2.8	0.90	1.7	−2.1	....	a	83.0	1.5
36.....	063128.13+045008.0	97.867223	4.835559	0.8	9.2	11.7	5.8	15.3	0.0	0.90	1.8	−2.4	....	a	83.7	1.3
52.....	063130.85+044847.3	97.878575	4.813144	0.9	9.7	13.4	6.8	23.6	0.1	0.89	1.8	−2.2	....	a	83.3	1.4
61.....	063132.25+050439.0	97.884410	5.077512	0.9	10.2	12.3	6.8	22.7	6.9	0.90	1.7	−2.0	....	a	63.1	2.7
68.....	063133.57+045233.3	97.889886	4.875920	0.6	6.7	8.2	4.1	4.8	2.9	0.89	1.7	−2.9	....	a	86.1	1.8
71.....	063134.14+044958.5	97.892258	4.832939	0.7	8.3	10.6	5.3	11.4	0.7	0.90	1.8	−2.5	....	a	84.7	1.1
83.....	063135.41+045813.0	97.897576	4.970293	0.6	5.4	5.8	3.4	2.2	4.5	0.90	1.5	−2.7	....	a	88.9	4.9
85.....	063135.75+050259.6	97.898985	5.049898	0.7	8.4	10.7	5.3	11.3	2.5	0.90	1.8	−2.5	....	b	79.9	1.6

Notes.—Col. (1): X-ray catalog sequence number, sorted by right ascension. Col. (2): IAU designation. Cols. (3) and (4): Right ascension and declination for epoch J2000.0. Col. (5): Estimated random component of position error, 1 σ, computed as (standard deviation of PSF inside extraction region)/(number of counts extracted)$^{1/2}$. Col. (6): Off-axis angle. Cols. (7) and (8): Estimated net counts extracted in the total energy band (0.5–8 keV) and average of the upper and lower 1 σ errors on col. (7). Col. (9): Background counts extracted (total band). Col. (10): Estimated net counts extracted in the hard energy band (2–8 keV). Col. (11): Fraction of the PSF (at 1.497 keV) enclosed within the extraction region. Note that a reduced PSF fraction (significantly below 90%) may indicate that the source is in a crowded region. Col. (12): Photometric significance computed as (net counts)/(upper error on net counts). Col. (13): Log probability that extracted counts (total band) are solely from background. Some sources have P_B values above the 1% threshold that defines the catalog because local background estimates can rise during the final extraction iteration after sources are removed from the catalog. Col. (14): Source anomalies: g = fractional time that the source was on a detector (FRACEXPO from `mkarf`) is <0.9; e = source on field edge; p = source piled up; s = source on readout streak. Col. (15): Variability characterization based on K-S statistic (total band): a = no evidence for variability ($0.05 < P_{K\text{-}S}$); b = possibly variable ($0.005 < P_{K\text{-}S} < 0.05$); c = definitely variable ($P_{K\text{-}S} < 0.005$). No value is reported for sources with fewer than 4 counts or for sources in chip gaps or on field edges. Col. (16): Effective exposure time: approximate time the source would have to be observed on axis to obtain the reported number of counts. Col. (17): Background-corrected median photon energy (total band). Table 3 is published in its entirety in the electronic edition of the *Astrophysical Journal*. A portion is shown here for guidance regarding its form and content.

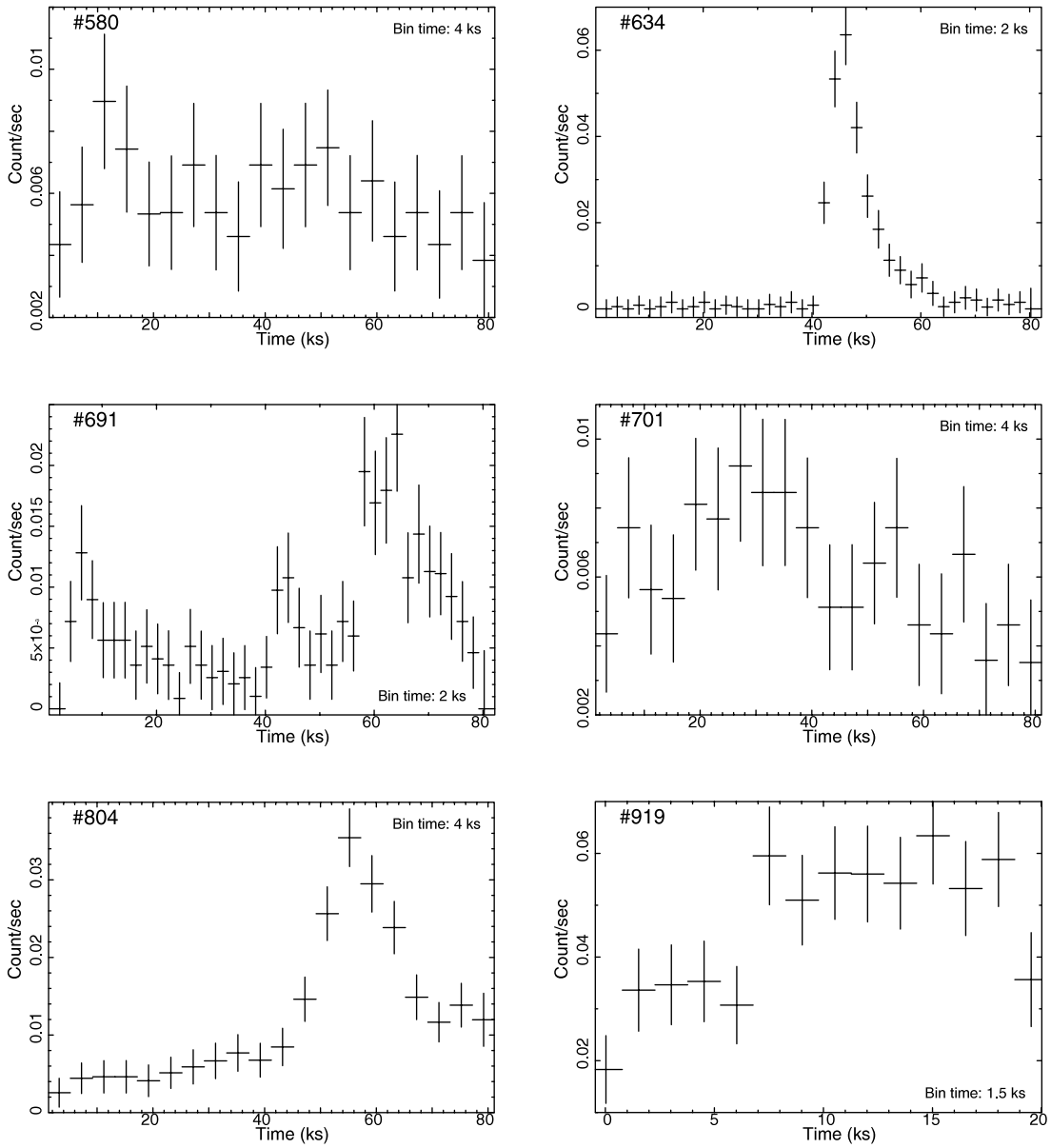

FIG. 4.—Light curves of sources with more than 500 counts that are significantly variable ($P_{\mathrm{K\text{-}S}} \leq 0.005$). The ACIS sequence numbers and bin sizes are marked.

3. IDENTIFICATION OF STELLAR COUNTERPARTS AND THEIR PROPERTIES

3.1. *Stellar Counterpart Matching and IR Diagrams*

We associate ACIS X-ray sources with optical and near-IR (ONIR) sources using positional coincidence criteria, as described in the Appendix of Broos et al. (2007).[8] The optical and infrared catalogs from recent literature and observations that we adopted for counterpart identification include *UBV* photometry of NGC 2244/Mon OB2 (Massey et al. 1995 = MJD95), *UBVI*Hα photometry of NGC 2244 (Park & Sung 2002 = PS02), *BVIR*Hα photometry of NGC 2244 (Berghöfer & Christian 2002 = BC02), the Whole-Sky USNO-B1.0 Catalog (Monet et al. 2003 = USNO), 2MASS All-Sky Catalog of Point Sources (Cutri et al. 2003[9] = 2MASS), and the University of Florida FLAMINGOS Survey of Giant Molecular Clouds.[10] The reference frame offsets between the ACIS fields (astrometrically aligned to the *Hipparcos* frame using 2MASS sources in the data reduction) and the catalogs are 0.4″ to MJD95, 0.3″ to PS02, 0.3″ to BC02, 0.2″ to USNO, and 0.2″ to FLAMINGOS. These offsets were applied before matching sources.

Likely associations between ACIS sources and ONIR sources are reported in Table 6; 712 of the 919 ACIS sources (77%) have an ONIR counterpart identified. Since Park & Sung (2002) provide the full list of their high-precision photometry, visual photometry is reported in the priority order of PS02, BC02, MJD95,

[8] Software implementing the matching algorithm is available in the TARA package at http://www.astro.psu.edu/xray/docs/TARA/.

[9] Available at http://irsa.ipac.caltech.edu/applications/Gator/.

[10] PI: Elizabeth A. Lada; details about the FLAMINGOS Survey can be found at http://flamingos.astro.ufl.edu/sfsurvey/sfsurvey.html. The instrument design and performance of FLAMINGOS are described in Elston et al. (2003). An overview of the instrument is also available at http://www.gemini.edu/sciops/instruments/flamingos1/flam1Index.html. The FLAMINGOS observations of the Rosette complex fields and IR data reduction are described in Román-Zúñiga (2006). Note that both *K* and *K*-short (K_s) filters are available in FLAMINGOS imaging mode, and the observations here are taken in *K* band.

TABLE 4

X-RAY SPECTROSCOPY FOR PHOTOMETRICALLY SELECTED SOURCES: THERMAL PLASMA FITS

Source[a]				Spectral Fit[b]			X-Ray Luminosities[c]					
Seq No. (1)	CXOU J (2)	Net Counts (3)	Signif (4)	$\log N_{\rm H}$ ($\rm cm^{-2}$) (5)	kT (keV) (6)	$\log {\rm EM}$ ($\rm cm^{-3}$) (7)	$\log L_s$ (ergs $\rm s^{-1}$) (8)	$\log L_h$ (ergs $\rm s^{-1}$) (9)	$\log L_{h,c}$ (ergs $\rm s^{-1}$) (10)	$\log L_t$ (ergs $\rm s^{-1}$) (11)	$\log L_{t,c}$ (ergs $\rm s^{-1}$) (12)	Notes[d] (13)
1.....	063114.36+045303.0	23.3	3.7	20.0	*2.0*	53.4	30.20	29.96	29.96	30.40	30.40	
2.....	063117.04+045228.3	32.0	4.5	$21.1^{+0.5}$	*2.0*	$53.7^{+0.2}_{-0.2}$	30.31	30.19	30.20	30.56	30.64	
3.....	063118.11+045511.8	12.4	2.5	$21.6^{+1.3}$	$2.8_{-2.6}$	53.4	29.78	30.03	30.06	30.23	30.39	
4.....	063118.29+045223.1	14.6	2.7	21.1	*2.0*	53.3	29.96	29.85	29.86	30.21	30.30	
5.....	063118.76+045207.6	9.7	2.1	$20.8^{+1.1}$	0.6	$52.9^{+0.8}$	29.73	28.33	28.34	29.75	29.85	
6.....	063119.27+045110.7	22.6	3.6	20.1	1.9	53.4	30.17	29.91	29.92	30.36	30.37	
7.....	063120.48+045023.4	98.9	8.5	$21.5^{+0.1}$	$1.7^{+0.8}_{-0.4}$	$53.8^{+0.07}_{-0.17}$	30.25	30.18	30.20	30.52	30.73	
8.....	063120.89+045003.8	599.7	22.8	21.4	0.6	54.4	31.11	29.86	29.89	31.13	31.51	H; HD 46056
9.....	063120.95+045322.7	14.5	2.6	21.0	3.4	53.0	29.70	29.81	29.81	30.06	30.11	
11.....	063121.46+045405.3	15.6	2.7	21.4	*2.0*	53.2	29.71	29.70	29.72	30.01	30.16	

NOTES.—Table 4 is published in its entirety in the electronic edition of the *Astrophysical Journal*. A portion is shown here for guidance regarding its form and content.

[a] For convenience cols. (1)–(4) reproduce the source identification, net counts, and photometric significance data from Table 2.

[b] All fits used the "wabs(apec)" model in XSPEC and assumed 0.3 $Z_\odot$ abundances (Imanishi et al. 2001; Feigelson et al. 2002). Cols. (5) and (6) present the best-fit values for the column density and plasma temperature parameters. Col. (7) presents the emission measure for the model spectrum, assuming a distance of 1.4 kpc. Quantities in italics were frozen in the fit. Uncertainties represent 90% confidence intervals. More significant digits are used for uncertainties <0.1 in order to avoid large rounding errors; for consistency, the same number of significant digits is used for both lower and upper uncertainties. Uncertainties are missing when XSPEC was unable to compute them or when their values were so large that the parameter is effectively unconstrained. Fits lacking uncertainties should be considered to be merely a spline to the data to obtain rough estimates of luminosities; actual parameter values are unreliable.

[c] X-ray luminosities are presented in cols. (8)–(12): s = soft band (0.5–2 keV); h = hard band (2–8 keV); t = total band (0.5–8 keV). Absorption-corrected luminosities are subscripted with a c; they are omitted when $\log N_{\rm H} > 22.5$ since the soft-band emission is essentially unmeasurable.

[d] 2T means a two-temperature model was used. H means the fit was performed by hand, usually because the automated fit yielded nonphysical results. Names of well-known OB counterparts are listed here for the convenience of the reader.

and USNO. USNO photometry is photographic with ~0.3 mag photometric accuracy (Monet et al. 2003). *JHK* magnitudes from FLAMINGOS photometry are reported if available for *Chandra* sources. The FLAMINGOS photometric data were zero-pointed to 2MASS. (See Román-Zúñiga et al. [2008] for details on photometry. A photometric catalog for optical stars in NGC 2244 is presented in Román-Zúñiga & Lada [2008], and the complete catalog from the FLAMINGOS survey of the Rosette will be reported in Román-Zúñiga et al. [2008].) For areas that were not covered by the FLAMINGOS survey and for bright stars that were saturated ($H < 11$ mag; Román-Zúñiga 2006), 2MASS photometry is reported. The SIMBAD and VizieR catalog services are used for complementary information. Notes to other published characteristics of the selected sources can be found in the table footnotes.

Figure 5 shows the NIR $J - H$ versus $H - K$ color-color diagram for 617 out of 919 *Chandra* stars with high-quality *JHK*

TABLE 5

X-RAY SPECTROSCOPY FOR PHOTOMETRICALLY SELECTED SOURCES: POWER-LAW FITS

Source[a]				Spectral Fit[b]			X-Ray Fluxes[c]					
Seq No. (1)	CXOU J (2)	Net Counts (3)	Signif (4)	$\log N_{\rm H}$ ($\rm cm^{-2}$) (5)	Γ (6)	$\log N_\Gamma$ (7)	$\log L_s$ (photons $\rm cm^{-2}\ s^{-1}$) (8)	$\log L_h$ (photons $\rm cm^{-2}\ s^{-1}$) (9)	$\log L_{h,c}$ (photons $\rm cm^{-2}\ s^{-1}$) (10)	$\log L_t$ (photons $\rm cm^{-2}\ s^{-1}$) (11)	$\log L_{t,c}$ (photons $\rm cm^{-2}\ s^{-1}$) (12)	Notes (13)
10.....	063121.28+045023.8	50.6	5.7	21.5	$1.4_{-0.9}$	$-5.6_{-0.5}$	29.80	30.45	30.46	30.54	30.62	
15.....	063123.59+045141.7	60.6	6.3	$21.5^{+0.5}$	$1.1^{+0.9}_{-0.6}$	$-5.9 + 0.5 - 0.4$	29.63	30.41	30.42	30.47	30.53	
26.....	063125.51+045252.2	45.5	5.4	20.0	2.0	−5.8	29.86	29.73	29.73	30.10	30.11	
31.....	063127.01+050205.0	14.3	2.3	22.3	1.5	−6.0	28.79	29.92	29.99	29.95	30.17	
84.....	063135.68+045322.2	26.9	4.1	$22.1^{+0.4}_{-0.7}$	$2.0_{-1.2}$	−5.7	29.21	29.98	30.03	30.04	30.33	
89.....	063136.33+045251.1	46.2	5.7	$21.9^{+0.3}_{-0.6}$	$1.8_{-0.9}$	−5.6	29.46	30.15	30.19	30.23	30.43	
91.....	063136.42+045602.8	12.2	2.5	22.3	1.5	−6.1	28.70	29.84	29.91	29.87	30.10	
94.....	063136.49+045959.0	10.6	2.2	$21.1^{+1.0}$	0.8	−6.8	28.90	29.72	29.72	29.78	29.80	
118.....	063139.24+050244.7	19.5	3.1	$22.1^{+0.3}$	1.3	−6.0	29.02	30.08	30.13	30.12	30.27	
126.....	063139.92+050059.4	47.1	5.8	$21.7^{+0.5}$	$1.3_{-0.8}$	$-5.8_{-0.4}$	29.54	30.31	30.33	30.38	30.47	

NOTES.—Table 5 is published in its entirety in the electronic edition of the *Astrophysical Journal*. A portion is shown here for guidance regarding its form and content.

[a] For convenience cols. (1)–(4) reproduce the source identification, net counts, and photometric significance data from Table 2.

[b] All fits used the "wabs(powerlaw)" model in XSPEC. Cols. (5) and (6) present the best-fit values for the column density and power-law photon index parameters. Col. (7) presents the power-law normalization for the model spectrum. Quantities in italics were frozen in the fit. Uncertainties represent 90% confidence intervals. More significant digits are used for uncertainties <0.1 in order to avoid large rounding errors; for consistency, the same number of significant digits is used for both lower and upper uncertainties. Uncertainties are missing when XSPEC was unable to compute them or when their values were so large that the parameter is effectively unconstrained. Fits lacking uncertainties should be considered to merely be a spline to the data to obtain rough estimates of luminosities; actual parameter values are unreliable.

[c] X-ray luminosities are presented in cols. (8)–(12): s = soft band (0.5–2 keV); h = hard band (2–8 keV); t = total band (0.5–8 keV). Absorption-corrected luminosities are subscripted with a c; they are omitted when $\log N_{\rm H} > 22.5$ since the soft-band emission is essentially unmeasurable.

TABLE 6

STELLAR COUNTERPARTS

X-RAY SOURCE		OPTICAL/INFRARED PHOTOMETRY															
Seq No. (1)	CXOU J (2)	USNO B1.0 (3)	MJD95 (4)	PS02 (5)	BC02 (6)	*U* (mag) (7)	*B* (mag) (8)	*V* (mag) (9)	*R* (mag) (10)	*I* (mag) (11)	Hα (mag) (12)	2MASS ID (13)	FLAMINGOS ID (14)	*J* (mag) (15)	*H* (mag) (16)	*K* (mag) (17)	PhCcFlg (18)
1.....	063114.36+045303.0	0948-0096209	...	...	...	...	19.33	...	17.15	17.37	...	06311429+0453032	...	14.49	13.64	13.45	AAA000
2.....	063117.04+045228.3	0948-0096228	...	...	...	...	20.75	...	18.32	16.59	...	06311696+0452281	...	14.94	14.17	13.85	AAA000
3.....	063118.11+045511.8	...	...	...	...	...	...	...	...	...	...	...	...	...	...	...	......
4.....	063118.29+045223.1	0948-0096235	...	...	...	...	19.47	...	16.79	15.67	...	06311825+0452234	...	14.53	13.53	13.22	AAA000
5.....	063118.76+045207.6	0948-0096241	503	...	14	13.36	13.36	12.90	12.38	12.91	12.57	06311881+0452089	...	11.98	11.77	11.71	AAA000
6.....	063119.27+045110.7	0948-0096246	...	...	...	...	19.39	...	16.84	15.52	...	06311925+0451121	...	14.35	13.58	13.29	AAA000
7.....	063120.48+045023.4	...	...	...	...	...	...	...	...	...	...	06312048+0450239	...	13.42	12.70	12.46	AAAc00
8.....	063120.89+045003.8	0948-0096261	454	...	15	7.64	8.37	8.22	8.16	8.09	8.13	06312087+0450038	063117+050522	7.84	7.84	7.82	AAA000
9.....	063120.95+045322.7	0948-0096264	...	...	...	...	19.50	...	17.52	16.43	...	06312100+0453238	063120+045323	14.93	14.14	13.97	AAA000
10.....	063121.28+045023.8	...	...	...	...	...	...	...	...	...	...	...	...	...	...	...	......

NOTES.—Cols. (1)–(2) reproduce the sequence number and source identification from Tables 2 and 3. Cols. (3)–(6) are the catalogs used for counterparts matching. For convenience, [MJD95] = Massey et al. (1995), [BC02] = Berghöfer & Christian (2002), [PS02] = Park & Sung (2002). Cols. (7)–(12) give available optical photometry. Cols. (13)–(17) provide NIR identifications and *JHK* photometry from FLAMINGOS (§ 3.1). Col. (18) lists the 2MASS photometric quality flags (Cutri et al. 2003). In the note on individual sources, [OI81] = Ogura & Ishida (1981), [LR04] = Li & Rector (2004), ProbMem = probability of being a cluster member from proper-motion data, [M82] = Marschall et al. (1982), [D06] = Dias et al. (2006). Table 6 is published in its entirety in the electronic edition of the *Astrophysical Journal*. A portion is shown here for guidance regarding its form and content.

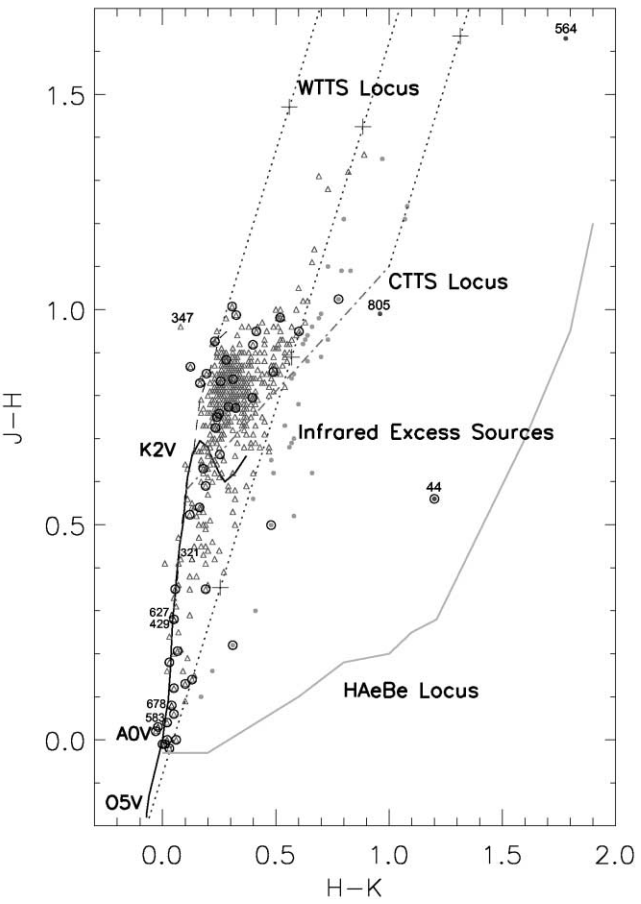

FIG. 5.—NIR $J - H$ vs. $H - K$ color-color diagram for 617 *Chandra* stars with high-quality photometry, from combined FLAMINGOS and 2MASS data (error in both $J - H$ and $H - K$ colors <0.1 mag). The filled circles and open triangles represent sources with significant K-band excess and sources without excess, respectively. The circles labeled with their sequence numbers from Table 2 represent three Class I objects. The triangles labeled 321, 429, 583, 627, and 678 are foreground stars, and 347 is likely a giant. Stars using 2MASS photometry are indicated with open circles. The solid and long-dashed lines denote the loci of MS stars and giants, respectively, from Bessell & Brett (1988). The dot-dashed line is the locus for classical T Tauri stars from Meyer et al. (1997), and the gray solid line is the locus for HAeBe stars from Lada & Adams (1992). The dashed lines represent the standard reddening vector with plus signs marking every $A_V = 5$ mag. Most *Chandra* sources are located in the reddening band defined by the left two dashed lines associated with Class III objects (*triangles*). To the right of this reddened band are 38 IR excess sources. [*See the electronic edition of the Journal for a color version of this figure.*]

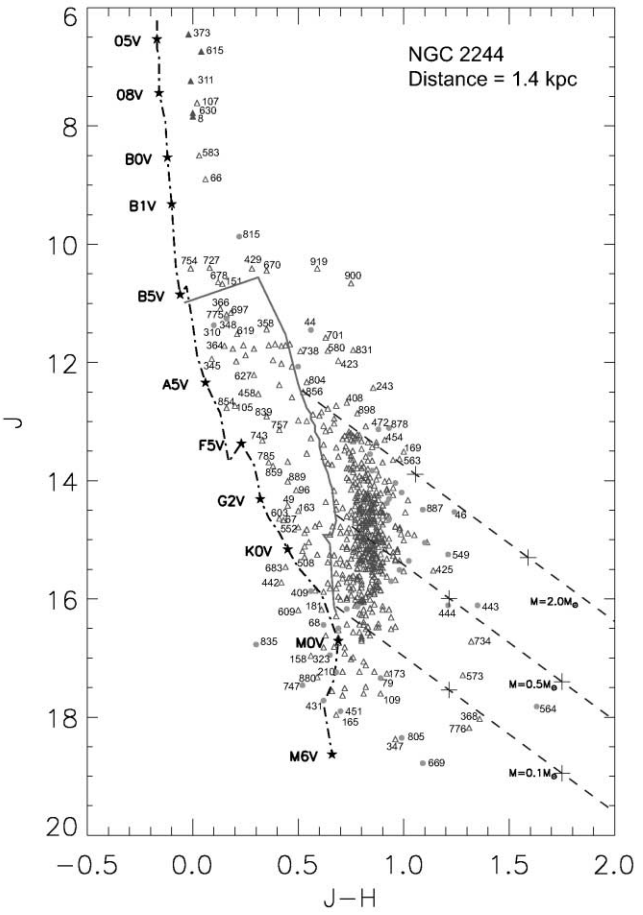

FIG. 6.—NIR J vs. $J - H$ CMD using the same sample and symbols as Fig. 5, except that known O stars are denoted as the filled triangles. ACIS source numbers are marked for some stars. The solid line is the 2 Myr isochrone for PMS stars from Siess et al. (2000). The dot-dashed line marks the location of ZAMS stars. The dashed lines represent the standard reddening vector with plus signs marking every $A_V = 5$ mag, and the corresponding stellar masses are marked. [*See the electronic edition of the Journal for a color version of this figure.*]

photometry (error in both $J - H$ and $H - K$ colors <0.1 mag) listed in Table 6. Most *Chandra* sources are located between the left two dashed lines, the color space associated with diskless young stars (Class III objects) that are reddened by interstellar extinction. We emphasize that while this region is usually filled with field star contaminants in NIR-only studies, here nearly all of these stars are cluster members (§ 3.2). A concentration of cluster members subjected to $A_V \sim 1$–2 mag (assuming late-type stars) is apparent, centered at $J - H = 0.25$, $H - K = 0.8$. To the right of this reddening band are 38 K-band excess sources,[11] defined as stars that have colors $(J - H) > 1.7(H - K) + 2\sigma(H - K)$. The presence of K-band excess is frequently used to identify stars still possessing inner disks that are relatively hot ($T \sim 1200$ K) and dusty. All except three of these stars occupy the color space between the middle and rightmost dashed lines; they are likely PMS stars with circumstellar accretion disks (Class II objects).

The three stars (44, 564, and 805) located beyond the rightmost dashed line show large color excess [$E(H - K) = 0.87$, 0.82, and 0.38, respectively]. Stars in this domain are likely surrounded by extended envelopes and hence are classified as candidate Class I protostars (Kenyon et al. 1993; Strom et al. 1995). Sources 44 and 564 are particularly interesting [$E(H - K) > 0.8$]. Source 44 was identified as a member of NGC 2244 (Ogura & Ishida 1981) and assigned spectral type B7 Ve (Verschueren 1991). It is further classified as a Herbig Be star in Li et al. (2002) based on the tenuous nebula seen in their Kitt Peak National Observatory (KPNO) Hα image, large [$V - 25$ μm] color, and its confirmed late B spectral type. Source 805 is very faint ($J \sim 18.5$, close to the FLAMINGOS imaging sensitivity limit) and may be a low-mass protostar or an embedded background object with large $H - K$ color (Froebrich et al. 2005).

Figure 6 shows the NIR J versus $J - H$ color-magnitude diagram (CMD) for the same stars shown in Figure 5. Known OB stars are located at the top and reddened from the ZAMS with $A_V \sim 1$ mag. Unlike NGC 6357 (Wang et al. 2007) and other more

[11] Note that the definition of K-band excess slightly varies when considered by different researchers. In Román-Zúñiga et al. (2008) a K-band excess star is required to have colors that lie above $J - H = 0.47(H - K) + 0.46$ (locus of the classical T Tauri stars [CTTSs]), in addition to requiring that the star is located to the right of the reddening band for ZAMS dwarfs. The region below the CTTS locus could include detections of unresolved galaxies. But for the IR counterparts to our X-ray–selected sample, this color space has little contamination from galaxies and likely contains HAeBe stars in the young cluster. Therefore, no further constraint is applied in defining the K excess.

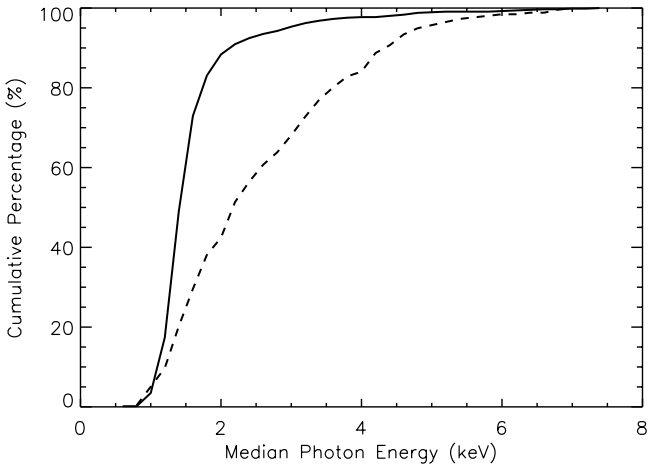

FIG. 7.—Cumulative distribution of the source hardness indicator, median photon energy, for *Chandra* sources with identified ONIR counterparts (*solid line*) and those without counterparts (*dashed line*). The sources with identified ONIR counterparts are considerably softer than the latter group.

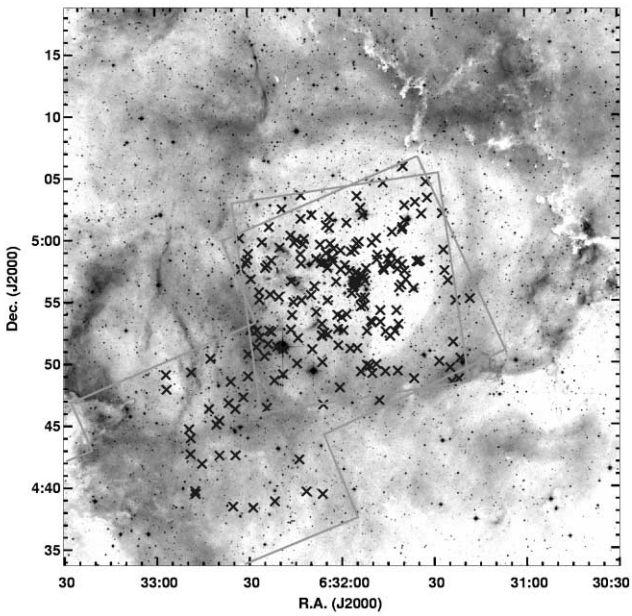

FIG. 8.—Spatial distribution of *Chandra* sources without identified ONIR counterparts. The background is the DSS *R*-band image. ACIS-I FOVs are shown.

heavily obscured clusters (Wolk et al. 2006; Broos et al. 2007), we do not locate any new candidate massive stars earlier than B0. However, two likely new B0–B2 stars (900 and 919) and a dozen new late B candidates are found.

Individual masses and reddening of the lower mass stars can be estimated assuming that they are reddened from the 2 Myr isochrone. Adopting a larger distance of $d = 1.6$ kpc does not have a significant effect here; the mass estimates for the low-mass stars are only affected by $\sim 0.1\ M_{\odot}$. The majority of ACIS stars appear to be concentrated around $0.7 \lesssim J - H \lesssim 1$ and $13 \lesssim J \lesssim 16$, consistent with F, G, K, and M stars ($0.1\ M_{\odot} \lesssim M \lesssim 2\ M_{\odot}$) reddened by 1 mag $\lesssim A_V \lesssim 2$ mag. Those showing *K*-band excess seem to have larger reddening compared to the Class III objects. Sources to the left of the 2 Myr isochrone are probably field stars older than the NGC 2244 population (see § 3.2). In addition, to the right of the ZAMS track, around 20 stars have inferred stellar masses $<0.1\ M_{\odot}$. The IR photometry for these $J > 17$ mag stars may be less reliable, especially the fainter ones that are close to the detection limit. These are likely a mixture of the lowest mass cluster members, background stars, and a few IR-luminous extragalactic sources. The high percentage of NIR excess sources among the faintest stars may not be real; Froebrich et al. (2005) have shown that background stars embedded in distant clouds have an overall larger $H - K$ color. Contamination by faint background IR sources is also discussed in Román-Zúñiga (2006).

The remaining $\sim$200 ACIS sources without matched counterparts are likely to be a mixture of newly discovered embedded members of the Rosette complex and distant background stars and extragalactic sources (see § 3.2 for estimated fractions). Cumulative distribution functions of the median photon energy are shown in Figure 7 for sources that have matched counterparts and those that do not have counterparts. The harder median photon energy of sources that do not have counterparts indicates that these sources are deeply embedded or behind the cloud ($A_V \gtrsim 10$ mag). The new low-mass cluster stars reveal themselves because of strong X-ray flares due to magnetic activity. Such X-ray–discovered stars are commonly found in the molecular clouds surrounding other clusters (Getman et al. 2005a; Wang et al. 2007; Broos et al. 2007). Some of these may be very young protostars with local absorption in an envelope or disk; Getman et al. (2007) found in IC 1396N that sources with $\log N_{\rm H} \gtrsim 23.0$ cm^{-2} are protostars with dense envelopes. Their spatial distribution (Fig. 8) shows that they are distributed around the bright stars and along the rims of the Rosette Nebula where infrared source identification may be challenging.

3.2. *Identification of Likely Contaminants*

As emphasized in § 1, stellar X-ray emission decays rapidly only after $\sim$100 Myr and shows only a small dependence of X-ray luminosity on disk accretion (Preibisch & Feigelson 2005; Preibisch et al. 2005; Telleschi et al. 2007). Therefore, X-ray surveys have very high efficiency in detecting disk-free PMS stars over MS stars, complementing traditional optical and infrared surveys of star-forming regions. We evaluate the level of contamination by extragalactic X-ray sources and Galactic disk stars following the simulations described in Getman et al. (2006) and Wang et al. (2007). The calculations indicate that $\lesssim$35 sources are extragalactic (§ 3.2.1), $\sim$20 are foreground, and $\sim$16 are background field stars (§ 3.2.2). These $\sim$70 contaminants constitute $\sim$8% of the 919 ACIS sources.

3.2.1. *Extragalactic Contaminants*

Following Getman et al. (2006), we construct Monte Carlo simulations of the extragalactic population by placing artificial sources randomly across the detector. We draw incident fluxes from the X-ray background $\log N - \log S$ distribution (Moretti et al. 2003), and power-law photon indices for the sources are assigned consistent with flux dependencies described by Brandt et al. (2001). The spectrum of each simulated source was passed through a uniform absorbing column density $\log N_{\rm H} \sim 21.9$ cm^{-2}, the H I column density through the entire Galactic disk in the direction of NGC 2244 (Dickey & Lockman 1990). After applying local background levels found in our ACIS image, we calculate the photometric significance of each fake source and then reject the weak extragalactic sources that would have fallen below our source detection threshold. The simulations suggest that $\sim$80 extragalactic sources may be detected in our ACIS-I field and $\sim$35 may have photometric significance Signif ≥ 2.0 (col. [12] in Table 2). The true number is probably smaller as we did not account for the patchy distribution of molecular cloud material. The best candidates for the extragalactic contaminants are those

sources whose X-ray spectra are best fitted by a power law, do not have bright ONIR counterparts, and do not display the characteristic PMS X-ray flares.

3.2.2. *Galactic Stellar Contamination*

Monte Carlo simulations of the Galactic stellar population expected in the direction of our ACIS fields ($l = 206.3, b = -2.1$) were examined, based on the stellar population synthesis model of Robin et al. (2003; henceforth the Besançon model).[12] In addition to the smooth absorption component provided in the model, we added a local absorption at $d = 1.4$ kpc with a low $A_V \sim 1$ mag, as inferred from the average NIR reddening of *Chandra* sources shown in Figure 6. Within the ACIS FOV, the Besançon model predicts ~850 foreground MS stars ($d < 1400$ pc) and ~4300 background MS stars, giants, and subgiants within the FLAMINGOS imaging sensitivity limit around $J < 19$ mag.

About 25% of the foreground stars in the Besançon simulation have ages less than 1 Gyr, the younger population that could be detected in X-ray surveys. Most reside at distances from 0.8 to 1.4 kpc; ~54% are M stars, ~28% are K stars, ~13% are G stars, and 3% are more massive. Following Getman et al. (2006), we convolved the Besançon model populations with the XLFs of stars in the solar neighborhood measured from *ROSAT* surveys (Schmitt et al. 1995; Schmitt 1997; Hünsch et al. 1999). Luminosities were adjusted to account for the different *ROSAT* and *Chandra* spectral bands following the stellar hardness-luminosity relation (Güdel et al. 1998). Following the same procedure we used for extragalactic sources (§ 3.2.1), we applied our ACIS detection process to these simulated field stars. A typical Monte Carlo run predicts that 16–20 foreground stars will be detected in the ACIS-I exposures of NGC 2244.

Five optical counterparts to our X-ray stars are identified as foreground stars based on their known spectral types and positions in photometric diagrams. These are sources 321, 429, 583, 627, and 678. Proper-motion data (Marschall et al. 1982; Dias et al. 2006) also suggest that they have low probability of being member stars of the cluster. In the NIR CMD, there are ~30 stars located between the 2 Myr isochrones and the ZAMS track. Those close to the 2 Myr isochrones are still consistent with being members due to uncertainty in the age and distance of the cluster. About 15 stars close to the MS track are more likely to be unrelated foreground MS stars (Getman et al. 2006). Available X-ray absorption columns derived from spectral fits mostly require $\log N_{\rm H} = 20.0$ cm^{-2}, suggestive of being foreground candidates.[13] Their probabilities of being members derived from proper-motion data range between 0% and 80%, which are less conclusive. With the above five confirmed foreground stars, altogether 20 optical stars[14] are noted as the best candidates for foreground stars in the Table 6 footnotes. This number is quite consistent with the Besançon simulated foreground population.

The Besançon model is again convolved with XLFs to simulate the number of stars behind the Rosette star-forming region that may enter our X-ray sample. The model predicts ~18% F dwarfs, ~41% G dwarfs, ~33% K dwarfs, ~1% M dwarfs, and ~6% giants. We use the dwarf XLFs established for the solar neighborhood (Schmitt et al. 1995; Schmitt 1997) and adopt the XLF for giants obtained from Table 2 of Pizzolato et al. (2000). Typical runs of simulations result in ~11 dwarfs and ~5 giants that are detectable in our *Chandra* observation. To the left of the ZAMS track in the CMD and for $J > 18$, there are 16 stars[15] whose locations match the Besançon model predicted background population of MS stars, subgiants, and giants, which we note as best candidates for background stars in Table 6.

4. GLOBAL PROPERTIES OF THE STELLAR CLUSTER

4.1. *X-Ray Luminosity Function and Initial Mass Function*

As noted in Feigelson et al. (2005), the XLF (which is directly measured here) can be considered to be the convolution of the IMF (which is unknown) and the X-ray luminosity–mass (L_X-M) correlation (which is measured in the COUP studies; Preibisch et al. 2005). Using the best-studied Orion Nebula Cluster (ONC) XLF (COUP XLF) and IMF as a calibrator, the NGC 2244 XLF can be used to probe the IMF of the stellar cluster and to estimate the total X-ray–emitting population. Such a population analysis has been made for Cep OB3b, NGC 6357, and M17 (Getman et al. 2006; Wang et al. 2007; Broos et al. 2007). In the following XLF analysis, we use the hard-band XLF rather than the total-band XLFs, since the unknown soft component of heavily absorbed X-ray sources can introduce a large uncertainty in both the observed and absorption-corrected total-band X-ray luminosity.

By counting the number of sources in different X-ray luminosity bins, we construct the absorption-corrected hard-band (2–8 keV) XLF ($L_{h,c}$) for all unobscured NGC 2244 X-ray sources (Med $E \leq 2.0$ keV) with derived X-ray luminosities in Figure 9*a*. Here we exclude the five known foreground stars and OB stars with spectral types earlier than B3 to be consistent with the Orion cool star sample. The absorption-corrected hard-band fluxes ($F_{h,c}$) derived from XSPEC spectral fitting are used to obtain luminosities assuming a distance of 1.4 kpc. As the template, we also show the XLF of the COUP unobscured population (839 cool stars; Feigelson et al. 2005).

The NGC 2244 XLF is largely consistent with the COUP XLF, suggesting an NGC 2244 population comparable to the ONC. However, at $\log L_{h,c} \gtrsim 29.8$ ergs s^{-1} the slope of the NGC 2244 XLF seems steeper than the COUP XLF. At $\log L_{h,c} = 30.9$ ergs s^{-1}, the NGC 2244 bin is short nine stars compared to the ONC XLF; the luminosity bins at $\log L_{h,c} = 29.5$–29.7 ergs s^{-1} are ~40 stars higher than the ONC XLF. Admittedly these deviations from the ONC XLF are not significant (2 σ), more closely following the shape of the ONC than the Cep B or the M17 XLF does (see Fig. 9*b*). The apparent steeper slope is not an artifact of our distance estimate or detection completeness limit. We comfortably detect 15 count sources at any off-axis location; the X-ray luminosity of the detected sources is roughly $\log L_t \sim 29.4$ ergs s^{-1} (corresponding to ~0.5 $M_\odot$ from the L_X-M relation) and $L_{h,c} \sim 29.2$ ergs s^{-1}. The luminosity bins with the steep slope seen in the NGC 2244 XLF are much brighter than the completeness limit.

A few possible extrinsic reasons may account for the slope deviation from the ONC XLF. First, while the lognormal COUP XLF represents the best data and provides a good observational template, the underlying physics and the variations from it among clusters remain to be explored. There is evidence that the XLF may not be identical in all regions (see review by Feigelson et al.

[12] These calculations are made with the Web service provided by the Robin et al. (2003) group at Besançon at http://bison.obs-besancon.fr/modele.

[13] Spectral fits to low-count sources can give $N_{\rm H}$ values with large uncertainties; hence, we do not use low $N_{\rm H}$ to identify foreground sources. Low absorption columns are considered supporting evidence for foreground stars suggested by their locations in the NIR CMD. The spatial distributions of the low-$N_{\rm H}$ sources with high counts (>30 counts) and with low counts (<30 counts) are similarly dispersed through the field, consistent with being part of the foreground population.

[14] They are associated with *Chandra* sources 49, 67, 96, 105, 129, 163, 321, 429, 552, 583, 603, 627, 678, 743, 757, 785, 839, 854, 859, and 889.

[15] They are sources 68, 157, 158, 181, 226, 253, 323, 325, 347, 409, 442, 583, 609, 747, 835, and 880.

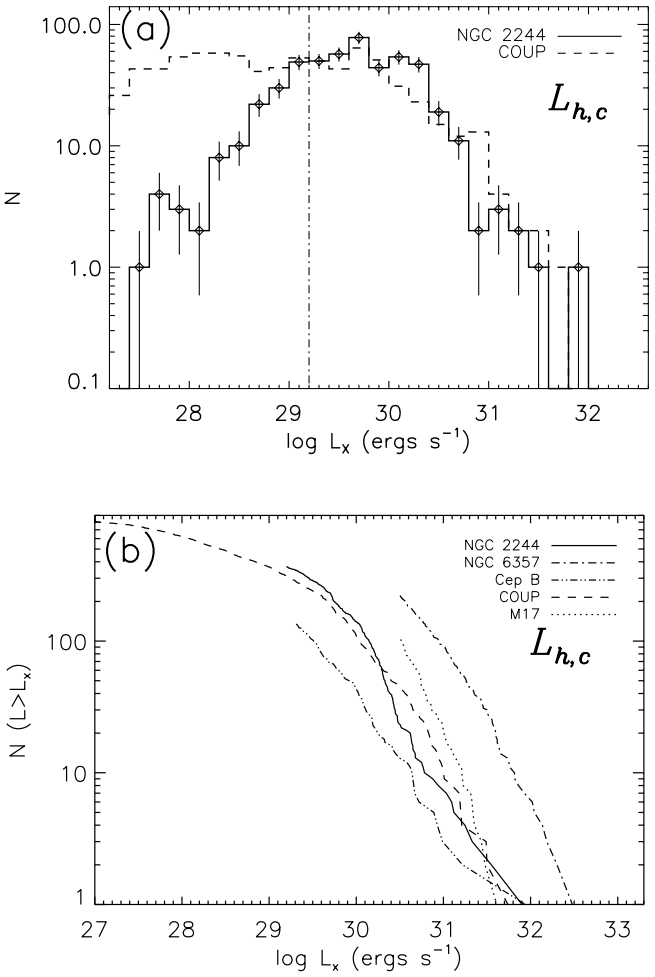

FIG. 9.—(*a*) XLF constructed from the absorption-corrected hard-band (2.0–8.0 keV) X-ray luminosity $L_{h,c}$ for the unobscured NGC 2244 population (*solid line*) and the COUP ONC unobscured cool star population (*dashed line*; Feigelson et al. 2005). The vertical line denotes the estimated completeness limit for the NGC 2244 population. (*b*) Cumulative distribution of X-ray luminosities for the unobscured NGC 2244 X-ray sources, as well as the unobscured populations in COUP, Cep B/OB3b (age $\sim$ 1–3 Myr; Getman et al. 2006), NGC 6357 (age $\sim$ 1 Myr; Wang et al. 2007), and M17 (age $\sim$ 1 Myr; Broos et al. 2007). The distributions for NGC 2244, NGC 6357, Cep B, and M17 are truncated at their completeness limits, log $L_{h,c} \sim$ 29.2, 30.4, 29.3, and 30.4 ergs s^{-1}, respectively.

2007). Figure 9*b* suggests that the XLFs of Cep B and M17 may vary from the ONC XLF in different ways. The L_X-M correlation is derived from the very young ONC but may vary for the older clusters like NGC 2244. Second, the exclusion of some hot stars to construct an XLF comparable to the COUP XLF could implicitly affect the resulting XLF. We examined luminosities (log $L_{h,c}$) of these OB stars, which mostly contribute to the luminosity bins around log $L_{h,c} \sim$ 30.0 ergs s^{-1}; an XLF including them still shows the observed deviation from the ONC.

There are two possibilities intrinsic to the NGC 2244 cluster that may be responsible for the apparent steeper slope: (1) the NGC 2244 population is the same as the COUP population, but there is an excess of $\sim$50 stars in the luminosity range 30.0 $\lesssim$ log $L_{h,c} \lesssim$ 30.4 (solar mass stars as inferred from the L_X-M relation); or (2) the NGC 2244 population is $\sim$1.2 times larger than the COUP population, but NGC 2244 is $\sim$20 stars deficient in stars with 30.4 $\lesssim$ log $L_{h,c} \lesssim$ 31.0 (intermediate-mass stars). In either case, the NGC 2244 XLF deviates from a scaled version of the COUP XLF in a manner similar to that seen in the Cep B/OB3b field studied by Getman et al. (2006).

To improve the statistics, remove possible binning effects, and further investigate how the NGC 2244 XLF compares to that of the ONC and other clusters, we derive the cumulative distribution of X-ray luminosities for the unobscured NGC 2244 X-ray sources, as well as the unobscured COUP, Cep B/OB3b (age $\sim$ 1–3 Myr; Getman et al. 2006), NGC 6357 (age $\sim$ 1 Myr; Wang et al. 2007), and M17 (age $\sim$ 1 Myr; Broos et al. 2007) populations. The resulting cumulative XLFs are shown in Figure 9*b*. To avoid confusion caused by incompleteness in detections, we cut off the cumulative XLFs at the corresponding completeness limit for each region (see Fig. 9). At a given X-ray luminosity above the completeness limit, the ratio between the cumulative numbers of sources from two populations reflects the relative scaling between the two populations that are more luminous than this limit. As a result, the unobscured population of NGC 6357, M17, and Cep B is $\sim$5 times, $\sim$3 times, and $\sim$0.4 times the size of the unobscured ONC population, respectively. These are consistent with previously reported values.[16] The cumulative XLF of NGC 2244 closely follows the COUP XLF, although the deviation found in Figure 8 (deficit at 30.4 $\lesssim$ log $L_{h,c} \lesssim$ 31.0 and excess at log $L_{h,c} \lesssim$ 30.4) can still be clearly seen. Depending on the treatment of this deviation, the NGC 2244 population ranges from 1.0 times to 1.2 times the ONC population.

Further investigations were made to examine the possible excess of sources with 30.0 ergs $s^{-1} \lesssim$ log $L_{h,c} \lesssim$ 30.4 ergs s^{-1}. To identify a previously unknown cluster in the field that may contribute extra stars to NGC 2244, we inspected the spatial distribution of sources that have luminosities in the excess bins, but we did not find any apparent clustering. To test whether this excess comes from contamination of X-ray–bright nonmembers, we removed candidate contaminants (foreground stars, background stars, extragalactic sources) as suggested in § 3.2 and reconstructed the XLF. The number drop mainly appears in low-luminosity bins while the excess is still significant at 30.0 ergs $s^{-1} \lesssim L_{h,c} \lesssim$ 30.4 ergs s^{-1}. Therefore, we conclude that excluding candidate contaminants would not alter the XLF, since they do not contribute much to the high-luminosity bins that characterize the X-ray–emitting population.

4.2. *Initial Mass Function and K-Band Luminosity Function*

To examine whether the deviation in the XLF is a reflection of an intrinsic anomalous IMF in the NGC 2244 cluster, we perform two tests on the IMFs using NIR data. One experiment is to use the location of X-ray stars in the IR CMD to derive their masses and construct an approximate IMF. The exact mass will not be as accurate as measured from spectral types and an H-R diagram, but their statistical distribution should be sufficient for our interest here. If there is indeed an excess of X-ray sources with log $L_{h,c} \sim$ 30.0–30.4 ergs s^{-1} (option 1 in § 4.1), from the empirical L_X-M relation (Preibisch et al. 2005), we would expect to see an excess of stars around a solar mass. Figure 10 shows the IMF constructed from NIR estimated masses for unobscured COUP stars and for NGC 2244 stars. No excess is apparent for stars in the solar mass range, after the ONC IMF (Muench et al. 2002) is scaled to match the NGC 2244 IMF. Instead, a deficit of intermediate-mass stars around 2–3 $M_\odot$ in the X-ray–selected sample is apparent (option 2 in § 4.1).

[16] In NGC 6357, log $L_{h,c}$ is $\sim$0.5 dex higher than the other clusters because candidate OB stars are included in the sample (Wang et al. 2007). Note that, although the unobscured population of NGC 6357 is larger than that of M17, the obscured population in M17 is significantly larger than that of NGC 6357 (Broos et al. 2007), which makes the estimated total populations of the two clusters comparable.

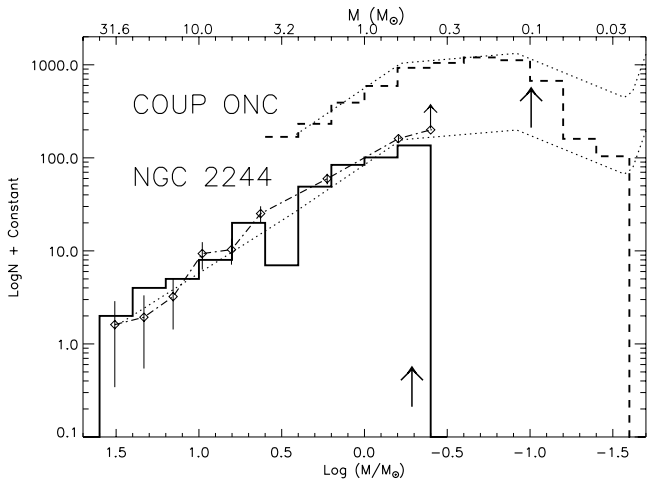

FIG. 10.—Comparison between IMFs of the NGC 2244 X-ray stars (*solid line*) and COUP ONC stars (*dashed line*) using NIR photometry derived stellar masses. The dotted lines show the ONC IMF (Muench et al. 2002) and its scaled version to match the NGC 2244 IMF. The dot-dashed line is the NGC 2244 IMF estimated using the KLF derived from 2MASS data. The arrows indicate the approximate mass completeness limits for the NGC 2244 and ONC X-ray stars and the mass completeness limit for the KLF derived from 2MASS data. Note that the 2MASS completeness limit is the same as our *Chandra* completeness limit in stellar mass. The incomplete bins in the NGC 2244 KLF/IMF are omitted.

A second test is to obtain a statistical sample of cluster members and construct a KLF (Lada & Lada 1995) following the Cep B/OB3b KLF analysis in Getman et al. (2006). We used 2MASS K_s data to construct the KLF since it was spatially complete toward NGC 2244 and it is photometrically complete to a similar mass limit as our *Chandra* data for the Rosette. A control field from 2MASS centered at $(\alpha, \delta) = (06^{\rm h}30^{\rm m}00^{\rm s}, +03^\circ45'00'')$ (J2000.0) is used for background population subtraction (extinction toward this control field and in the foreground of NGC 2244 is low; for its 2MASS color-color diagram see Li 2005). The resulting KLF is similar to that derived by Li (2005) with a power-law slope $d \log N(K_s)/dK_s \sim 0.3$. To get the IMF, we convert K_s magnitude to $\log M$ using the 2 Myr theoretical isochrone. The relation between K_s and $\log M$ from the theoretical isochrone (Siess et al. 2000) can be approximated well with a power law as demonstrated by Getman et al. (2006). The resulting IMF derived from K-band star counting (dot-dashed line in Fig. 10) is consistent with the IMF estimated from NIR properties of *Chandra* sources (solid histogram in Fig. 10). Note that the mass derived using K magnitude as a proxy for photospheric luminosity can be biased toward higher mass for K excess sources. However, our IMF estimated from KLF is justified; the fraction of K excess sources in our sample is low and the IMF inferred from the KLF is coarsely binned [$\Delta \log (M/M_\odot) \sim 0.2$] to account for the effect of K excess on the estimated mass.

This KLF suggests that our X-ray sample is largely complete down to $\sim 0.5\ M_\odot$, consistent with the mass limit estimated from the X-ray completeness limit. It also suggests that our X-ray–selected sample is missing $\sim$20 intermediate-mass stars around $3\ M_\odot$. It is not surprising that the detection efficiency of intermediate-mass stars in the X-ray band is not as deep as in optical or IR (Schmitt et al. 1985). The X-ray production mechanism is not well understood for stars in the intermediate-mass range (§ 5.2). In many cases of X-ray detections of intermediate-mass stars, the X-ray emission in fact comes from a low-mass companion to the intermediate-mass star. Compared to the ONC, some of the intermediate-mass stars in NGC 2244 may be X-ray–quiet because of the absence of low-mass companions. This is reflected as the deficit of $\log L_{h,c} \sim 30.4$–31.0 erg s^{-1} sources in the XLF. The dynamical evolution history of the young cluster might result in a lower fraction of intermediate-mass stars with secondaries. Surveys of intermediate-mass member stars in NGC 2244 to measure their multiplicity, such as the binarity study of Sco OB2 intermediate-mass stars by Kouwenhoven et al. (2007), are needed. Under this assumption, the "excess" of $\log L_{h,c} \sim 30.0$–30.4 erg s^{-1} sources would then be the result of a slightly larger population of NGC 2244 stars compared to that of the ONC.

Based on all the above analysis, we conclude that the unobscured X-ray–emitting NGC 2244 population is about 1.2 times larger than the known unobscured population in ONC, or $\sim$1000 stars with $\log L_t > 27.0$ ergs s^{-1} (the COUP detection limit). The obscured population, estimated from similar XLF scaling, is $\sim$500 stars. Given that the total COUP sample accounts for $\sim$75% of the ONIR sample of the ONC in Hillenbrand & Hartmann (1998), we estimate that the total size of the NGC 2244 stellar population is around 2000. Li (2005) gives a census of $\sim$1900 NGC 2244 members estimated from the spatially complete 2MASS analysis.

Although the massive end of the stellar complement in NGC 2244 was well known from early studies (e.g., Ogura & Ishida 1981), the low-mass populations were poorly identified. Perez (1991) suggested that there may not be $M < 4\ M_\odot$ stars in the NGC 2244 cluster. Perez (1991), Massey et al. (1995), and Park & Sung (2002) investigated the IMF for NGC 2244 in optical and reported a top-heavy IMF with a flat power-law slope $\Gamma[d \log N(\log M)/d \log M] \sim -0.7$, although Park & Sung (2002) are cautious due to the incompleteness of their intermediate- and low-mass population. Indeed, their optical sample becomes incomplete for stars with masses lower than $\sim 3\ M_\odot$. In comparison to the traditional IMF studies, our high-sensitivity X-ray sample of stars largely benefits from our robust membership criteria and our ability to identify the low-mass members in a reliable manner. The IMF slope obtained from the X-ray–selected membership, which is nearly complete to $0.5\ M_\odot$, gives $\Gamma \sim -1.1$ instead of $\Gamma \sim -0.7$, consistent with the Orion IMF.

4.3. *Spatial Structure of the Stellar Cluster*

The morphology of young clusters, including dependency on stellar mass, provides clues for cluster formation and dynamical evolution. As morphological studies based on optical or infrared samples are complicated by patchy extinction, nebular contamination, confusion with field stars, and bias toward stars retaining protoplanetary disks, the spatial distributions of X-ray–identified stars in populous young clusters should be excellent laboratories to explore their origins and dynamical evolution. For example, an aspherical shape or clumpy distribution would reflect unequilibrated initial conditions, while a spherical shape with mass segregation would indicate well-developed virialization (Clarke et al. 2000). In the Orion A cloud, the ONC, NGC 2024, and associated molecular filaments have flattened shapes (Lada 1991; Feigelson et al. 2005), which have been attributed to global gravitational collapse of an elongated cloud (Hartmann & Burkert 2007). In contrast, the rich NGC 6357 and M17 clusters appear spherical but with subclusters that may reflect distinct (perhaps triggered) subcluster formation (Wang et al. 2007; Broos et al. 2007). The absence of mass segregation can reflect either a young stellar system that has not yet achieved dynamical relaxation or a mature system where many of its massive members have been ejected by few-body interactions in the core (Pflamm-Altenburg & Kroupa 2006).

It was recognized in the 2MASS study by Li (2005) that the apparent center of the large-scale annulus (see Fig. 1*b*) defining the

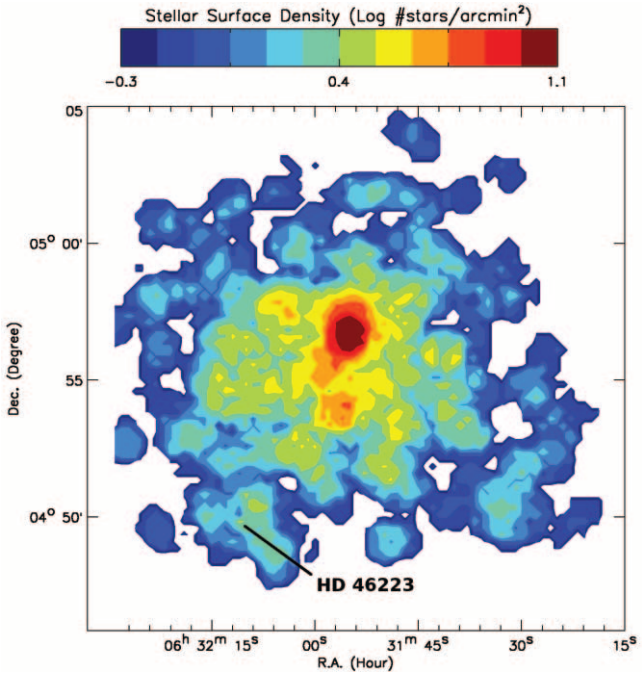

FIG. 11.—Stellar surface density map for the unobscured stellar population in NGC 2244. The cluster shows a spherical structure that extends 8′ in diameter. The highest concentration of stars is around R.A. = $06^h31^m55^s$, decl. = $+04^\circ56'34''$, the location of HD 46150. A secondary density enhancement is seen centered at R.A. = $06^h31^m56^s$, decl. = $04^\circ54'10''$. The O4 star HD 46223 is mostly isolated.

optical Rosette Nebula at $(\alpha, \delta) = (06^h31^m56^s, +04^\circ59'56'')$ (Ogura & Ishida 1981) is offset from the center of the IR surface density distribution at $(\alpha, \delta) = (06^h31^m59.9^s, +04^\circ55'36'')$. He interprets this offset as a projection effect where the Rosette Nebula resembles a tilted cylindrical cavity in the molecular cloud (see models in Celnik 1986). The distribution of the Class II sources in a recent *Spitzer* IRAC-MIPS survey of NGC 2244 (Balog et al. 2007) shows good agreement with the 2MASS data. Here our *Chandra* data show that the stellar concentration around HD 46150 is offset from the larger stellar distribution, irrespective of its relation to interstellar matter. The off-center massive star HD 46223 is further discussed in § 4.4.

A "center" must be defined for structural analysis. In NGC 2244, the highest concentration of X-ray stars appears around the second most massive star, HD 46150 (O5 V), at $(\alpha, \delta) = (06^h31^m55^s, +04^\circ56'34'')$. We therefore treat HD 46150 as the center for our radial profile analysis of this high-density region in § 4.3.2, although we are aware of the asymmetrical distribution of X-ray stars as noted above: HD 46150 lies about 2′ northwest of the IR center defined in the 2MASS study (Li 2005).

4.3.1. *Morphology and Substructures*

Figure 11 shows a smoothed map of the stellar surface density for 572 lightly obscured (median photon energy $\lesssim$2 keV) NGC 2244 X-ray stars. This map of smoothed spatial distribution is constructed following Wang et al. (2007) and Broos et al. (2007). A similar smoothing technique has been applied to 2MASS data to identify large-scale structure of the entire Rosette complex (Li 2005; Li & Smith 2005a, 2005b). A $\sim 20' \times 20'$ grid is created to cover the stellar positions, and at each position the total number of sources within a 0.5′ radius sampling kernel is counted to estimate the smoothed stellar density. Only sources covered by both ObsID 1874 and ObsID 3750 are considered to guarantee roughly equal X-ray sensitivity throughout the field. The heavily obscured sources are omitted because many of them are expected to be background AGNs.

The cluster shows an approximately spherical structure that extends 8′ (3.2 pc) in diameter, centered at $(\alpha, \delta) = (06^h31^m59^s, 04^\circ55'30'')$. This center, as well as the large-scale structure and substructure seen in the X-ray–sampled cluster (Fig. 11), is in good agreement with the results derived from the surface density of *K* excess stars in the FLAMINGOS study (Román-Zúñiga et al. 2008). It also matches the center defined from the 2MASS star count (Li 2005) and the center defined from the *Spitzer* Class II sources (Balog et al. 2007). The large-scale north-south asymmetry can be attributed to the off-center placement of HD 46150. The primary concentration is seen around HD 46150. Five of these stars were noted by Sharpless (1954) as a visual compact subcluster, but we find $\sim$50 stars extending to a radius of 1′ around this massive star. The central stellar surface density here is $\sim$700 stars pc^{-2}; recall that this value is restricted to stars with masses above $\sim 0.5\ M_\odot$ due to X-ray sensitivity limits.

A secondary density enhancement of $\sim$15 X-ray sources (about a 3 σ enhancement) is seen 3′ south of HD 46150 at $(\alpha, \delta) = (06^h31^m56^s, +04^\circ54'10'')$. Different sampling scales are tested, and this substructure persists for smoothing kernels with radii $<1'$. The local density peak here has six stars tightly clustered within 20″; it is also apparent in the optical Hα image and the 2MASS K_s image (Fig. 12 and Li 2005). Assuming that they are lightly obscured late-type stars, the reddening indicated by their NIR colors is $A_V \sim 1$ mag, similar to that of the NGC 2244 cluster. Their NIR estimated spectral types range from F to M if they are located at the same distance as NGC 2244.

The existence of both substructures, around HD 46150 and 3′ to the south, is direct evidence that the NGC 2244 cluster has not attained dynamical equilibrium. But perhaps most remarkable is the absence of companions around the most massive cluster member, HD 46223 (O4 V). Nine X-ray sources lie within 1′ of HD 46223 compared to $\sim$50 around HD 46150. One possible explanation for the isolation of HD 46223 is that it was ejected by dynamical interactions within the HD 46150 subcluster. However, it does not exhibit high proper motion (§ 4.4) and it seems unlikely that such a massive member, rather than less massive members, would be ejected at high velocity. We note, however, that an O4 supergiant has been reported to be probably ejected from Cyg OB2 (Comeron & Pasquali 2007). Radial velocity measurement of HD 46223 will be valuable to evaluate the ejection scenario.

The spatial distribution of the NGC 2244 sources exhibits some common characteristics and notable differences when compared to M17 (see § 3.1 in Broos et al. 2007). They both show the highest density of stars close to massive O stars, and the concentration is largely spherical. However, the concentration in M17 is around the known early O stars in NGC 6618, while in NGC 2244 the concentration is not around its massive star with the earliest spectral type (HD 46223) but with another O star, HD 46150. Both clusters show distinct substructures: in M17 an obscured small cluster is found (M17-X), which is seen as an elongation of the central cluster in M17; an unobscured substructure is also found in NGC 2244. M17 shows a triggered stellar population along the shock front and the eastern edge of the M17-SW molecular core (south bar in Jiang et al. 2002). To the southeast of NGC 2244, a sequence of triggered embedded clusters also exists along the midplane of the RMC (Phelps & Lada 1997). The different appearances of the triggered populations are related to the geometric configuration of the dense giant molecular clouds relative to the H II regions. The V-shaped M17 is an edge-on blister H II region emerging from the surrounding molecular materials,

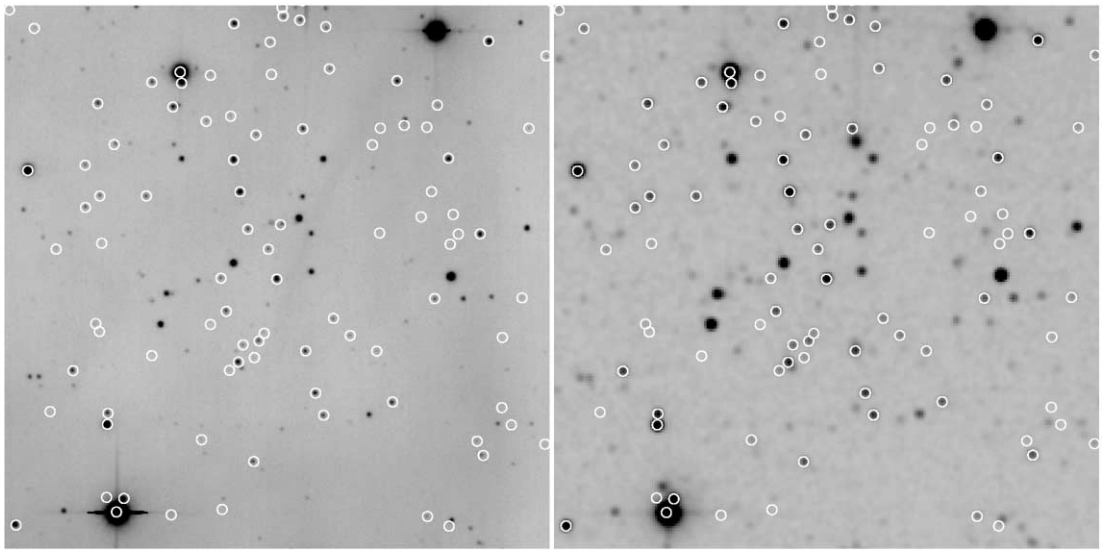

FIG. 12.—KPNO Hα image (Li & Rector 2004) and 2MASS K_s image of the secondary overdensity of stars seen in Fig. 11. The overlaid circles mark the ACIS sources. The $3.5' \times 3.5'$ images are both centered at R.A. $= 06^h31^m56^s$, decl. $= 04^\circ54'16''$.

while NGC 2244 is located in an expanding H II bubble at the tip of the elongated RMC.

4.3.2. *Radial Density Profile*

The radial density profile for the NGC 2244 cluster, centered at the stellar density peak around HD 46150, is shown in Figure 13 with comparison profiles from optical/NIR and X-ray studies of the ONC (Hillenbrand & Hartmann 1998; Feigelson et al. 2005) and from our X-ray study of Pismis 24 in NGC 6357 (Wang et al. 2007). The radial profile of NGC 2244 has two distinctive components: a power-law structure around HD 46150 extending 1.5′, and a structure with a flat core and steeper drop-off extending from 1.5′ to 8′. The power-law structure is centered on, but is much more extended than, the ~20″ X-ray–resolved subcluster around HD 46150 shown in Figure 3. NGC 6357 and perhaps the ONC have a similar radial profile with approximately the same power-law slope (Fig. 13).

Figure 14 shows the inferred radial density profiles in physical size units (parsecs) for the three clusters, where the star densities are scaled to their estimated true densities based on the comparison of the XLFs shown in Figure 9*b*. The stellar density of NGC 2244 has been scaled to 1.2 times the ONC population (§ 4.1), and NGC 6357 to 5 times the ONC population (Wang et al. 2007). Omitting the central r^{-2} power-law structures, the profiles of these two clusters can be fitted as isothermal spheres (King 1962) with core radii $r_c = 1.2$ and 1.4 pc, respectively.

4.4. *Mass Segregation*

The concentration of massive cluster members at the center and lower mass members at larger radii from the cluster center is commonly observed in rich young star clusters (e.g., Carpenter et al. 1997; Hillenbrand & Hartmann 1998; Adams et al. 2001). Schilbach et al. (2006) investigate mass segregation in over 600 open clusters with a wide range of ages. For their youngest clusters with ages ~5 Myr, some show mass segregation whereas others do not.

Mass segregation can occur as a natural consequence of dynamical relaxation. Details of the process have been debated. For

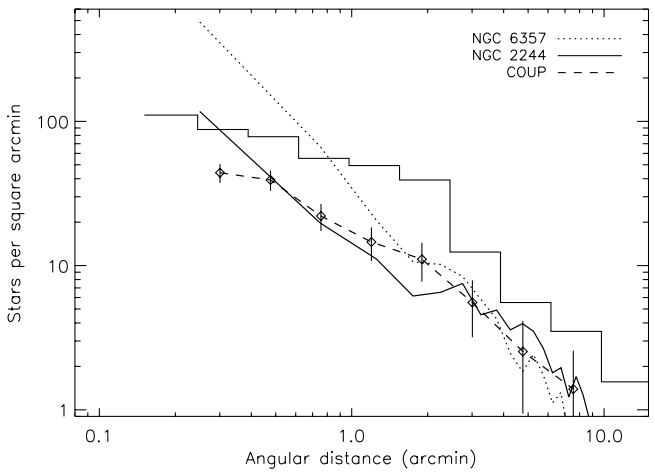

FIG. 13.—Observed radial density profiles of the NGC 2244 cluster, the ONC from COUP studies (Feigelson et al. 2005), and the NGC 6357 region from our *Chandra* ACIS observation (Wang et al. 2007). The histogram shows the radial density profile of the ONC from ONIR studies (Hillenbrand & Hartmann 1998). The 1 σ Poisson error is shown for the COUP ONC.

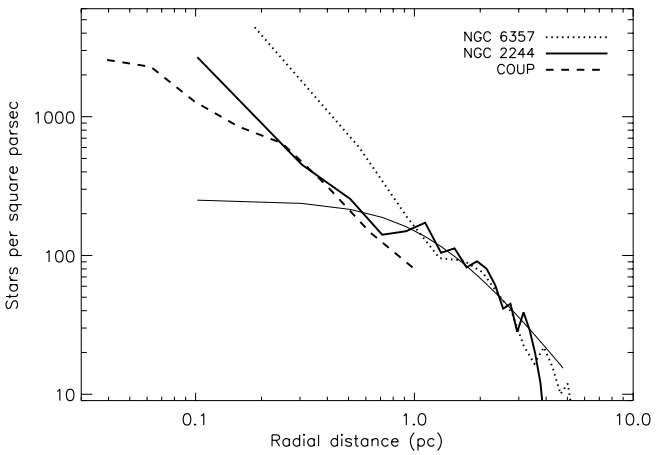

FIG. 14.—Radial density profiles (*thick lines*) in physical scales for the same three clusters, where the stellar densities of NGC 2244 and NGC 6357 have been scaled to 1.2 times and 5 times the ONC population, respectively, based on the XLF analysis. The thin line represents a King model profile for the outer portion of NGC 2244.

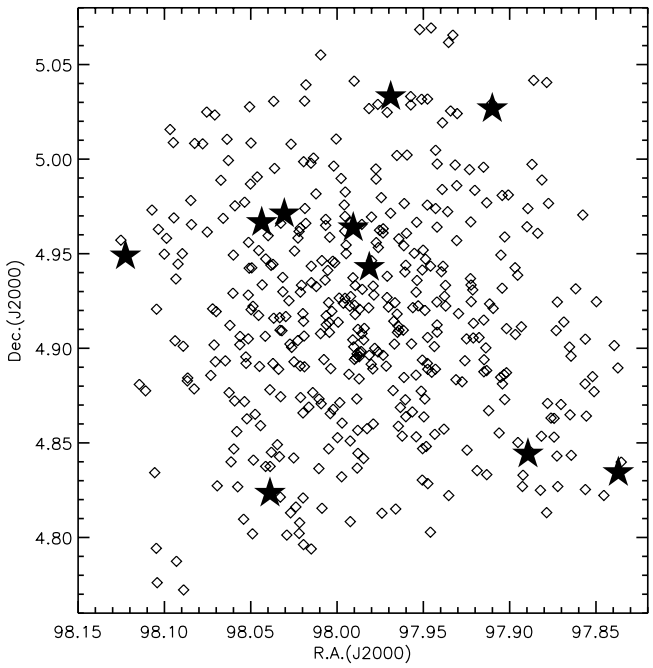

FIG. 15*a*

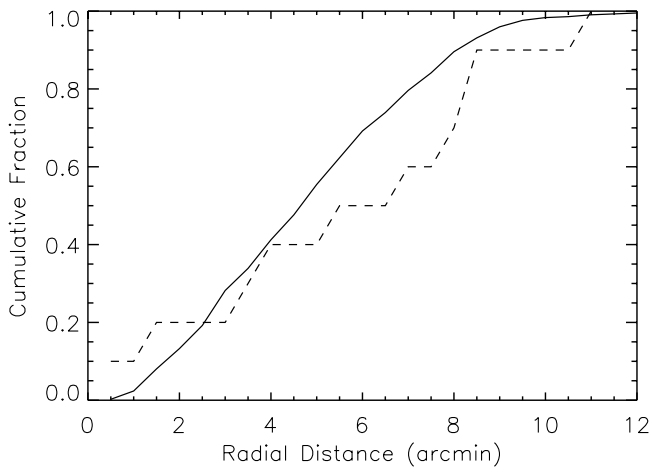

FIG. 15*b*

FIG. 15.—(*a*) Spatial distribution of the massive stars (NIR estimated mass $M \gtrsim 8\ M_{\odot}$; *filled stars*) and the low-mass stars ($M \lesssim 2\ M_{\odot}$; *open diamonds*) in NGC 2244, using our X-ray–selected sample. (*b*) Cumulative radial distributions for the massive stars (NIR estimated mass $M \gtrsim 8\ M_{\odot}$; *dashed line*) and the low-mass stars ($M \lesssim 2\ M_{\odot}$; *solid line*).

the ONC Trapezium, some researchers argue that the dense collection of ~10 OB stars is an imprint of initial conditions (Binney & Tremaine 1987; Bonnell & Davies 1998), while others argue that the core has collapsed and many OB stars have been ejected (Pflamm-Altenburg & Kroupa 2006). McMillan et al. (2007) suggest a model of sequential mergers of mass-segregated subclusters. Bonatto et al. (2006) found that the M16 cluster, with age ~1.3 Myr, has an overall relaxation timescale around ~20 Myr, yet shows some degree of mass segregation at this young age.

In NGC 2244 in the Rosette Nebula, the O stars are not highly concentrated, as shown in Figure 15*a* (see also Fig. 1*a*). The earliest O-type (O4 V) star in the cluster, HD 46223, has a rather puzzling location in the cluster near the southeast boundary of the nebula. Its proper motion is fairly small ($\mu_{\alpha} = -0.2$ mas yr^{-1}, $\mu_{\delta} = 0.4$ mas yr^{-1}; Zacharias et al. 2004), which does not suggest ejection from the cluster center. The issue of mass segregation has not been extensively investigated for this 2 Myr old cluster in the literature, mainly because the low-mass population was not adequately identified. With the proper motions and membership probabilities of stars in the NGC 2244 region derived from photographic plate data, Chen et al. (2007) suggest that the cluster shows evidence of mass segregation.

Figure 15*b* shows the cumulative radial distributions for the massive stars with NIR-estimated masses $M \gtrsim 8\ M_{\odot}$ and for the X-ray–identified low-mass stars ($M \lesssim 2\ M_{\odot}$). The distributions appear very similar, and a K-S test of the two distributions does not show significant difference. Thus, mass segregation is not present in NGC 2244 within our FOV.

We estimate a two-body dynamical relaxation time $t_{\rm relax}$ for the NGC 2244 cluster (e.g., Bonatto et al. 2006): $t_{\rm relax} \approx (N/8 \ln N) t_{\rm cross}$, where $t_{\rm cross} = 2R/v_{\rm disp}$ is the characteristic crossing time for a star to travel through the cluster with radius R and velocity dispersion $v_{\rm disp}$. Adopting $R \sim 4$ pc from the full cluster extent in Figure 14, a rough estimate for the unmeasured velocity dispersion $v_{\rm disp} \sim 3$ km s^{-1} (Binney & Tremaine 1987), and $N \sim 1900$ stars (§ 4.1), we obtain $t_{\rm relax} \sim 30$ Myr for NGC 2244. As the cluster age is <10% of this relaxation time, no significant mass segregation is expected from two-body dynamical interactions. If we consider only stars within the estimated core radius $r_c = 1.2$ pc, then $t_{\rm relax} \sim 9$ Myr, which is still considerably larger than the age of the cluster.

The absence of mass segregation is thus consistent with standard dynamical theory and implies that NGC 2244 (unlike some other clusters) was not formed with a central concentration of massive stars. The main challenge for explaining the dynamical state of NGC 2244 is the difference between the dominant member HD 46150, which has a rich compact subcluster, and HD 46223, which is mostly isolated.

Similar to NGC 2244, Broos et al. (2007) show that many other massive stars are scattered all over the ACIS-I field in M17, in addition to the concentration in NGC 6618. ACIS source 51 is one of the most massive stars in the field, yet it sits >6′ from the center of the cluster. For comparison, HD 46223 is about ~7′ south of HD 46150 and ~5′ south of the cluster center in NGC 2244. Not all massive stars are participating in the mass segregation seen in NGC 6618. One possible explanation is that the O stars are not all coeval. Indeed, several massive protostars have been found in M17 (e.g., Nielbock et al. 2001; Chini et al. 2004, 2005). Together with the presence of an ultracompact H II region there, these young massive stars establish that the massive populations are not all the same age in M17. Massive stars to the east might be older and belong to a wider OB association, while source 51, for example, might be younger. This could also be the case in NGC 2244. The late O stars are scattered as in M17. HD 46223 may be younger and not part of the same population as NGC 2244's central cluster.

4.5. *X-Ray Stars with Infrared Excess Disks*

X-ray–selected samples have several advantages over optical and IR samples (see review by Feigelson et al. 2007). X-ray emission arises from stellar magnetic activity, which is enhanced

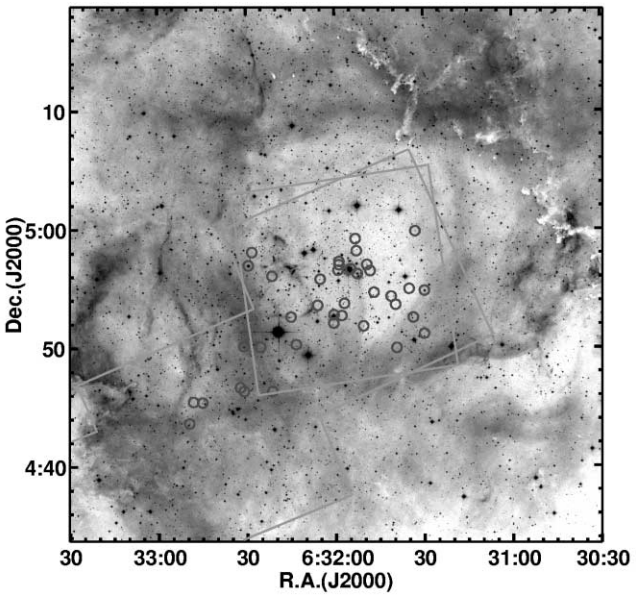

FIG. 16.—Spatial distribution of 38 sources with significant NIR color excess (*circles*). The northern part of the nebula seems deficient in NIR excess sources. The boxes outline the FOVs of the multiple ObsIDs.

10^1–10^4 above MS levels for stars during the entire age range of interest (<0.1 to >10 Myr); thus, X-ray surveys suffer only a small number of field and extragalactic contaminants (∼8% in observations of rich massive clusters), which are usually identifiable (§ 3.2). They naturally deliver a nearly disk-unbiased sample of young stars.[17] The main disadvantage of typical X-ray surveys is their incompleteness in detecting the lowest mass objects, which can be identified in high-sensitivity IR images. The complementary nature of the *Chandra* and IR data will provide the best census to date for the young stellar population of NGC 2244. It is worth noting that because the different disk indicators in the IR trace thermal emission from circumstellar materials of different temperatures, the inferred disk fraction of a young cluster generally increases when measured in longer IR wavelengths (e.g., Lada et al. 2004). For example, Haisch et al. (2001b) show that *JHK* observations alone are not sensitive enough to detect circumstellar disks in a complete and unambiguous manner. They find that 21% of the sources in the IC 348 cluster have *K*-band excess disks; the disk fraction rises to 65% when using *JHKL* IR excess emission. In this subsection we focus on the X-ray–selected sample of stars with *K*-band excesses.

The spatial distribution of 38 X-ray stars with *K*-band excesses attributed to inner protoplanetary disks (§ 3.1) is shown in Figure 16. Ten of these young stars cluster around HD 46150 (O5 V), and a few are around HD 259135 (B0.5 V).

A deficit of color excess stars in the northern part of the nebula is seen: none of them are located in the northern part of the cluster where HD 46149 (O8.5 V) is located. This region is also devoid of dust emission in the *IRAS* image (Cox et al. 1990). The deficit of disky stars cannot be attributed to photoevaporation by OB stellar UV radiation and winds since a grouping of them is found around HD 46150. We consider two explanations for this asymmetry. First, Li (2005) suggested that the Rosette Nebula is open 30° north of the line of sight. As gas and dust stream away from the H II region (as in M17; T03), the stars in this region may have undergone a faster inner disk dissipation so that their disks no longer show *K*-band excess. Second, the star formation in NGC 2244 may have proceeded over a considerable time span along the north-south direction, with the older population in the northern region. Similar spatial age patterns have been found in other young clusters (e.g., Cep OB3b; Burningham et al. 2005).

For the ∼2 Myr old NGC 2244 cluster, using our X-ray–selected sample with high *JHK* photometric quality (largely complete to 0.5 $M_\odot$), we derive an overall disk frequency of ∼6% for *Chandra* stars with mass $M \gtrsim 0.5\ M_\odot$ (assuming a presence of ∼20 foreground field stars). The disk fraction is ∼10% for stars with mass $M \gtrsim 2.0\ M_\odot$ and ∼5% for stars with mass $0.5\ M_\odot \lesssim M \lesssim 2.0\ M_\odot$. Using a large *Chandra* sample similar to that studied here, Wang et al. (2007) reported a low fraction of K_s band excess among intermediate-mass stars in the young massive star-forming region NGC 6357 (∼1 Myr old), and a similar result is reported for M17 (∼1 Myr old) in Broos et al. (2007). These are consistent with the findings that optically thick circumstellar disks are already rare among the intermediate-mass PMS stars with ages less than a few Myr and suggest that the disks are short lived for the massive stars (e.g., Hillenbrand et al. 1993; Natta et al. 2000). It has been suggested that the disks around earlier type stars may evolve faster than around later type stars based on studies of the IR excess fraction as a function of spectral type in a few clusters (Lada et al. 2000, 2006; Haisch et al. 2001a).

Li (2005) used the 2MASS NIR sample after background population subtraction to derive a K_s excess disk fraction of ∼20.5% above mass ∼0.8 $M_\odot$ for NGC 2244. The discrepancy between our results reflects the different criteria in selecting excess sources: their K_s excess sources included 2MASS sources with large photometric error. With high-quality FLAMINGOS *JHK* photometry data, Román-Zúñiga et al. (2008) derive a lower *K* excess fraction of ∼10% for $K < 15.75$ stars, although it remains slightly higher than the IR excess fraction in our X-ray–selected sample. Their sample covers a larger mass range, probably down to 0.1–0.2 $M_\odot$ depending on extinction (Román-Zúñiga et al. 2008).

Balog et al. (2007) present a *Spitzer* survey of NGC 2244 covering 3.6–24 μm and estimate that the overall disk fraction in the cluster is 44.5% using the IRAC data (and MIPS data if available). The total cluster population in their FOV (0.5 deg^2), including the cluster members without disks, is estimated by subtracting the average background population, whereas our sample identifies the diskless stars from their elevated X-ray emission. But the discrepancy between our results is mainly due to the fact that *Spitzer* mid-IR observations are much more sensitive to circumstellar dust than *K*-band excesses. The overall IR excess fraction among NGC 2244 *Chandra*-selected stars will be studied with a deep *Spitzer* survey (PI: Bouwman) and compared to the IR-only determined excess fraction, aiming to evaluate the different samples of young stars selected through IR colors and those identified in X-rays. A similar study has already taken place in the Serpens cloud core (Winston et al. 2007), which analyzed combined *Spitzer* and *Chandra* observations of the embedded stellar cluster.

The overall low *K* excess disk frequency seen here (∼6% for *Chandra* stars with mass $M \gtrsim 0.5\ M_\odot$; ∼10% for FLAMINGOS stars with mass $M \gtrsim 0.1\ M_\odot$), at a cluster age of 2 Myr, may imply a faster disk dissipation while the cluster is immersed in the hostile environment of UV radiation and strong stellar winds of many massive stars. In clusters of similar age but without the presence

[17] There may be additional complications: X-ray–selected PMS samples suffer a small bias against accreting stars in the 0.5–8 keV band because Class II systems are on average ∼2 times fainter than Class III systems (Preibisch et al. 2005; Telleschi et al. 2007), and there may also be a small bias toward accretion systems in the soft <1 keV band due to emission at the accretion shock. However, accretion variations do not cause X-ray variations in the *Chandra* band (Stassun et al. 2006). These are minor effects considering that the XLF spans 28 ergs s^{-1} < log L_X < 32 ergs s^{-1} and is dominated by flare emission. See discussion in Feigelson et al. (2007).

of O stars, the *K*-band excess fractions appear higher. For example, in the 2.3 Myr old IC 348 cluster Lada & Lada (1995) find that 20% of the stars ($M \gtrsim 0.08\ M_\odot$, estimated from the *K* magnitude completeness limit) have *K* excess disks. The recent *Spitzer* observations of IC 348 find a total disk frequency of ~50% among stars with mass $M \gtrsim 0.1\ M_\odot$ based on infrared excess between 3.6 and 8.0 μm (Lada et al. 2006; Muench et al. 2007), not significantly higher than the ~45% disk fraction in NGC 2244 reported in Balog et al. (2007). This implies that although the inner disks around the NGC 2244 stars may dissipate faster, there seems to be no difference in the overall disk dissipation.

However, Balog et al. (2007) did notice a lower disk fraction (27%) among stars close to the NGC 2244 O stars (separation $d < 0.5$ pc), hinting at a faster disk evolution near the massive stars. A number of observational and theoretical studies have already demonstrated the photoevaporation of disks by external radiation (e.g., O'Dell & Wong 1996; Johnstone et al. 1998; Hollenbach et al. 2000; Throop & Bally 2005). Balog et al. (2006) presented 24 μm images of three protoplanetary disks being photoevaporated around high-mass O stars, including one disk close to the O5 star HD 46150 in NGC 2244 with an estimated mass-loss rate of 10^{-10} to $10^{-8}\ M_\odot\ \mathrm{yr}^{-1}$. We do not detect X-ray emission from the IR point source in this cometary structure, likely due to its low mass. Based on the *Spitzer*-identified Class II and Class I sources, it is further suggested that the effect of massive stars on the circumstellar disks is significant in the immediate vicinity of the hot stars (Balog et al. 2007). Guarcello et al. (2007) reported evidence that the spatial distribution of the stars with a circumstellar disk in NGC 6611 is anticorrelated with the distribution of OB stars. Their findings also suggest that UV radiation from OB stars does have an impact on the evolution of the disks close to massive stars.

5. X-RAYS ACROSS THE MASS SPECTRUM

5.1. *X-Rays from Massive Stars*

One of the important discoveries of early *Einstein* observations was the soft X-ray emission from individual early-type O stars (Harnden et al. 1979). Most O-type stars were found to be soft X-ray emitters ($kT < 1$ keV) with X-ray luminosities $L_X \sim 10^{31}$–10^{33} ergs s^{-1}. A canonical relation between X-ray luminosity and bolometric luminosity of $L_X/L_{bol} \sim 10^{-7}$ was proposed and confirmed from *Einstein* and *ROSAT* observations (Pallavicini et al. 1981; Chlebowski et al. 1989). Berghöfer et al. (1997) extended the same relation down to stars of later spectral type (B1–B1.5). Recent *Chandra* studies of O7–B3 stars in Orion (COUP) found both a soft wind emission component and a hard flaring component in many OB stars, and a larger dispersion was found for late O and early B stars [$\log (L_X/L_{bol}) \sim -4$ to -8; Stelzer et al. 2005]. However, when only considering X-ray emission in the 0.5–2.5 keV band, Sana et al. (2006) derived a tight scaling law $\log (L_X/L_{bol}) = -6.91 \pm 0.15$ for O-type stars with a deep *XMM-Newton* observation of NGC 6231.

Wind shock models were developed to explain the X-ray emission from massive stars, where small-scale instabilities in radiatively driven stellar winds from massive stars produce shocks (Lucy & White 1980; Owocki et al. 1988; Owocki & Cohen 1999). To account for the observed X-ray emission line profiles and hard, variable continuum emission (e.g., Corcoran et al. 1994; Evans et al. 2004; Waldron et al. 2004; Stelzer et al. 2005), more complex models were invoked such as the magnetically channeled wind shock (MCWS) model (Babel & Montmerle 1997a, 1997b; ud-Doula & Owocki 2002). Gagné et al. (2005) show that the MCWS model with strong line-driven winds can adequately reproduce both the soft and the hard components in *Chandra* grating spectra of θ^1 Ori C (O6 V). In some cases, the anomalously hard and luminous X-ray component ($kT > 10$ keV and $L_h \sim 10^{33}$ ergs s^{-1}) implies close binarity, as powerful winds in two massive components collide and shock to produce very high energy X-rays (e.g., Pollock et al. 2005; Skinner et al. 2006; Broos et al. 2007). Schulz et al. (2006) observed a large X-ray outburst in θ^2 Ori A, which can be attributed to reconnection events from magnetic interactions between the binary stars.

Due to its richness in population, NGC 2244 offers an excellent opportunity to study X-ray emission in OB stars. Table 7 summarizes the detection/nondetection of O and early B-type stars in our observation, along with their optical, IR, and X-ray properties. *Chandra* spectra are shown in Figure 17. We detected all nine OB stars with spectral types B0.5 or earlier that were in the field. The two early O stars in NGC 2244 exhibit soft ($kT < 1$ keV) and strong ($L_X \sim 10^{32}$ ergs s^{-1}) X-ray emission as expected in the classical wind microshock regime. All of the 2.3 Myr old NGC 2244 O stars show soft X-ray emission ($kT < 1$ keV), which is similar to the soft thermal spectra seen in most O-type stars in other star-forming regions (e.g., Rauw et al. 2002; Rho et al. 2004; Skinner et al. 2005; Sana et al. 2006; Albacete Colombo et al. 2007). Nevertheless, unusual cases of O stars characterized by a hard spectrum have been reported in a number of observations (e.g., Gagné et al. 2005; Broos et al. 2007; Tsujimoto et al. 2007). Based on analysis of X-ray grating spectra of the Orion Trapezium stars, Schulz et al. (2003) proposed that the presence of hard X-ray emission indicative of hot coronal plasma ($kT > 1$ keV) indicates the presence of coronal magnetic fields. Linsky et al. (2007) compared the X-ray properties of young massive stars with known magnetic fields (e.g., θ^1 Ori C, O6 V, $t \sim 0.3$ Myr; M16 ES1) with older stars with weak or no magnetic fields (τ CMa, O9.5 I, $t < 12$ Myr; ζ Ori, O9 I, $t \sim 3$–5 Myr). The very young stars with magnetic fields show high coronal plasma temperatures ($kT \sim 2$–5 keV), which may be heated as in the MCWS model (Gagné et al. 2005), and the total X-ray luminosities are far larger than the expected X-ray luminosities from microshocks in the stellar winds. The absence of such a hot component in the X-ray spectra of the older massive stars (including our NGC 2244 O stars) might imply a timescale of the presence of coronal magnetic fields in the massive stars; the hot component may be restricted to stars much younger than 2 Myr. A detailed analysis of X-ray properties of a large sample of O stars will be required to link the magnetic fields in massive stars to the cluster ages.

We detected 6 out of 14 B stars with spectral types B1–B3. This low X-ray detection rate among B stars is consistent with other recent *Chandra* and *XMM-Newton* observations of massive star-forming regions (Wang et al. 2007; Broos et al. 2007; Sana et al. 2006). The X-ray emission from early B stars is consistently harder than that from the O stars (higher *kT* in Table 7), which suggests that unseen late-type companion stars rather than the B star itself are responsible (Stelzer et al. 2005).

The earliest exciting star in this complex, HD 46223, is of spectral type O4 V (Walborn et al. 2002). Its X-ray spectrum is adequately fitted by a soft $kT = 0.3$ keV single-temperature plasma subjected to $N_H = 4 \times 10^{21}\ \mathrm{cm}^{-2}$ absorption (Fig. 17). HD 46150 (O5 V) is the visually brightest early-type star in the cluster. A two-temperature plasma model fit ($kT_1 = 0.2$ keV, $kT_2 = 0.6$ keV) is needed to describe the X-ray spectrum, with an absorption column $N_H = 2.5 \times 10^{21}\ \mathrm{cm}^{-2}$. Their X-ray luminosities are similar, $L_{t,c} \sim 2.5 \times 10^{32}$ ergs s^{-1}. The light curves of the O stars are examined, and no variability is suggested by the K-S statistics. In contrast, both O4 V stars in M17 show a very hard plasma component ($kT > 10$ keV) and are nearly an order of

TABLE 7
X-Ray Properties of Cataloged OB Stars in NGC 2244

Optical/IR Properties					X-Ray Properties						
Name (1)	Spectral Type (2)	2MASS (3)	K (mag) (4)	$\log \tilde{L}_{\rm bol}$ ($L_\odot$) (5)	Seq No. (6)	$\Delta\phi$ (arcsec) (7)	NetCounts (8)	$\log N_{\rm H}$ ($\rm cm^{-2}$) (9)	kT (keV) (10)	$\log L_h$ (ergs $\rm s^{-1}$) (11)	$\log L_{t,c}$ (ergs $\rm s^{-1}$) (12)
HD 46223	O4 V((f))	06320931+0449246	6.68	5.7	615	0.2	1685	21.6	0.3	29.71	32.38
HD 46150	O5 V((f))	06315551+0456343	6.44	5.5	373	0.1	3589	21.4	0.6+0.2	30.48	32.34
HD 46485	O7 V	06335094+0431316	7.45	5.2	RMC 164	0.3	310	21.6	0.3+0.9	30.46	32.05
HD 46056	O8 V((f))	06312087+0450038	7.82	5.0	8	0.3	600	21.4	0.6	29.86	31.51
HD 46149	O8.5 V((f))	06315253+0501591	7.25	4.9	311	0.1	299	20.0	0.7	29.62	31.04
HD 258691	O9 V((f))	06303331+0441276	7.93	4.8	NFOV	...	...	...	...	...	...
HD 46202	O9 V((f))	06321047+0457597	7.72	4.8	630	0.1	333	21.2	0.3	28.75	31.11
HD 259238	B0 V	06321821+0503216	10.28	4.5	727	1.0	36	21.8	0.5	28.74	30.65
HD 46106	B0.2 V	06313839+0501363	7.62	4.4	107	0.2	186	21.4	0.4+1.4	29.81	30.94
MJD95	B0.5 V	06313708+0445537	12.20	4.3	NFOV	...	...	...	...	...	...
HD 259135	B0.5 V	06320061+0452410	8.12	4.3	476	0.7	186	20.6	1.6	30.04	30.57
IRAS 06309+0450	B0.5 V	06333749+0448470	8.64	4.3	NFOV	...	...	...	...	...	...
HD 259012	B1 V	06313346+0450396	8.79	4.0	66	0.6	275	21.1	2.5	30.75	31.12
HD 259105	B1 V	06315200+0455573	8.95	4.0	...	...	...	...	...	<28.3	<28.7
BD +04 1299s	B1 III	06320613+0452153	9.38	4.0	[a]	...	...	...	...	<28.3	<28.7
HD 46484	B1 V	06335441+0439446	6.86	4.0	NFOV	...	...	...	...	...	...
BD +05 1281B	B1.5 V	06315893+0455398	9.74	3.7	448	0.1	16	21.1	2.2	29.58	30.01
HD 259172	B2 V	06320259+0505086	10.08	3.5	NFOV	...	...	...	...	...	...
OI81 345	B2	06330656+0506034	11.20	3.5	NFOV	...	...	...	...	...	...
BD +04 1295p	B2.5 V	06313146+0450596	10.24	3.4	53	0.5	28	21.5	2.0	29.57	30.03
OI81 130	B2.5 V	06314789+0454181	10.87	3.4	...	...	...	...	...	<28.3	<28.7
OI81 190	B2.5 Vn	06315891+0456162	10.54	3.4	...	...	...	...	...	<28.3	<28.7
OI81 172	B2.5 V	06320984+0502134	10.43	3.4	...	...	...	...	...	<28.3	<28.7
OI81 274	B2.5 V	06322424+0447037	10.58	3.4	...	...	...	...	...	<28.3	<28.7
OI81 392	B2.5 V	06335056+0501376	9.99	3.4	NFOV	...	...	...	...	...	...
OI81 194	B3	06321548+0455203	10.96	3.2	697	0.1	62	21.2	3.6	30.16	30.45
MJD95	B3 V	06322249+0455342	13.48	3.2	...	...	...	...	...	<28.3	<28.7
HD 259268	B3	06322304+0502457	10.33	3.2	...	...	...	...	...	<28.4	<28.8
HD 259300	B3 Vp	06322939+0456560	9.34	3.2	815	0.3	60	21.5	1.4	29.88	30.54
OI81 334	B3	06325179+0447161	11.53	3.2	899	0.2	10	20.9	1.4	29.33	29.98
MJD95	B3 V	06331016+0459499	12.39	3.2	NFOV	...	...	...	...	...	...

Notes.—Col. (1): This list is obtained from Appendix A of T03, which gives optical cross identifications, positions, and spectral types. The stars are listed first in order of decreasing mass, and then by right ascension. OI = Ogura & Ishida (1981). Col. (2): Spectral types are from Ogura & Ishida (1981) and Massey et al. (1995). Cols. (3) and (4): Source numbers and K-band magnitudes are from the 2MASS All-Sky Point Source Catalog. Col. (5): Bolometric luminosities are estimated from calibrations of $L_{\rm bol}$ with spectral type, Martins et al. (2005) for O3–O9.5 stars and de Jager & Nieuwenhuijzen (1987) for B stars; no use is made of available photometry. Col. (6): *Chandra* source number, from Table 2. NFOV = object is not covered in the FOV, while ellipses indicate nondetection. HD 46485 is observed in Rosette Field 4 (RMC source 164; Paper II). Col. (7): Offset between the *Chandra* and 2MASS sources. Cols. (8)–(12): X-ray properties from Table 4: extracted counts after background subtraction; column density and plasma energy from fits to the ACIS spectra; observed hard-band luminosity (2–8 keV); inferred total-band luminosity corrected for absorption (0.5–8 keV). Upper limits to luminosities are estimated using the faintest sources in Table 4 and scaled with the corresponding exposure time.

[a] BD +04 1299s was reported as a detection in T03 (20 ks observation). However, the deep observation resolved this source into two X-ray sources. Both are separated by $\sim 2''$ from the optical position. Therefore, we do not report BD +04 1299s as a detection here.

magnitude brighter in their intrinsic full-band X-ray emission (Broos et al. 2007). If this hard emission is caused by close binarity or fossil magnetic fields, as suggested by Broos et al. (2007), then it is likely that the early O stars in NGC 2244 lack at least one of these features; their soft X-ray emission suggests that these are single O stars without close, massive companions and/or that they do not possess strong magnetic fields.

Berghöfer & Christian (2002) reported the X-ray and optical luminosities of NGC 2244 early-type stars from *ROSAT* PSPC and HRI observations and *BVI* photometry and concluded that they are consistent with the canonical relation $L_{\rm X}/L_{\rm bol} \sim 10^{-7}$. The $L_{\rm X}/L_{\rm bol}$ relation for OB stars in NGC 2244 determined from our *Chandra* data is shown in Figure 18. Statistical tests for the correlation between $L_{\rm X}$ and $L_{\rm bol}$ were performed using the ASURV survival analysis package (Isobe et al. 1986). To take into account the available upper limits, the generalized Kendall's tau correlation test for censored data is adopted. The null hypothesis (a correlation is not present) probability is $P < 0.01\%$, supporting a significant $L_{\rm X}$-$L_{\rm bol}$ correlation. As shown in Figure 18, as well as Table 7, the NGC 2244 O stars closely follow the ratio of X-ray to bolometric luminosities $L_{\rm X}/L_{\rm bol} \sim 10^{-7}$, although the B spectral type stars show larger (yet still <0.5 dex) scatter. For comparison, previously reported $L_{\rm X}$ versus $L_{\rm bol}$ values for additional OB stars from the massive star-forming regions Orion (1 Myr; Stelzer et al. 2005), NGC 6357 (1 Myr; Wang et al. 2007), and M17 (1 Myr; Broos et al. 2007) are also shown in Figure 18. The overall scatter in $L_{\rm X}/L_{\rm bol}$ is considerably smaller for O stars from different clusters (~2 orders of magnitude) than for B stars (~4 orders of magnitude).

5.2. *X-Rays from Intermediate-Mass Stars*

X-ray emission from intermediate-mass stars with spectral types mid-B to A is unexpected since no X-ray production mechanism is known; they lack strong stellar winds and convective surfaces

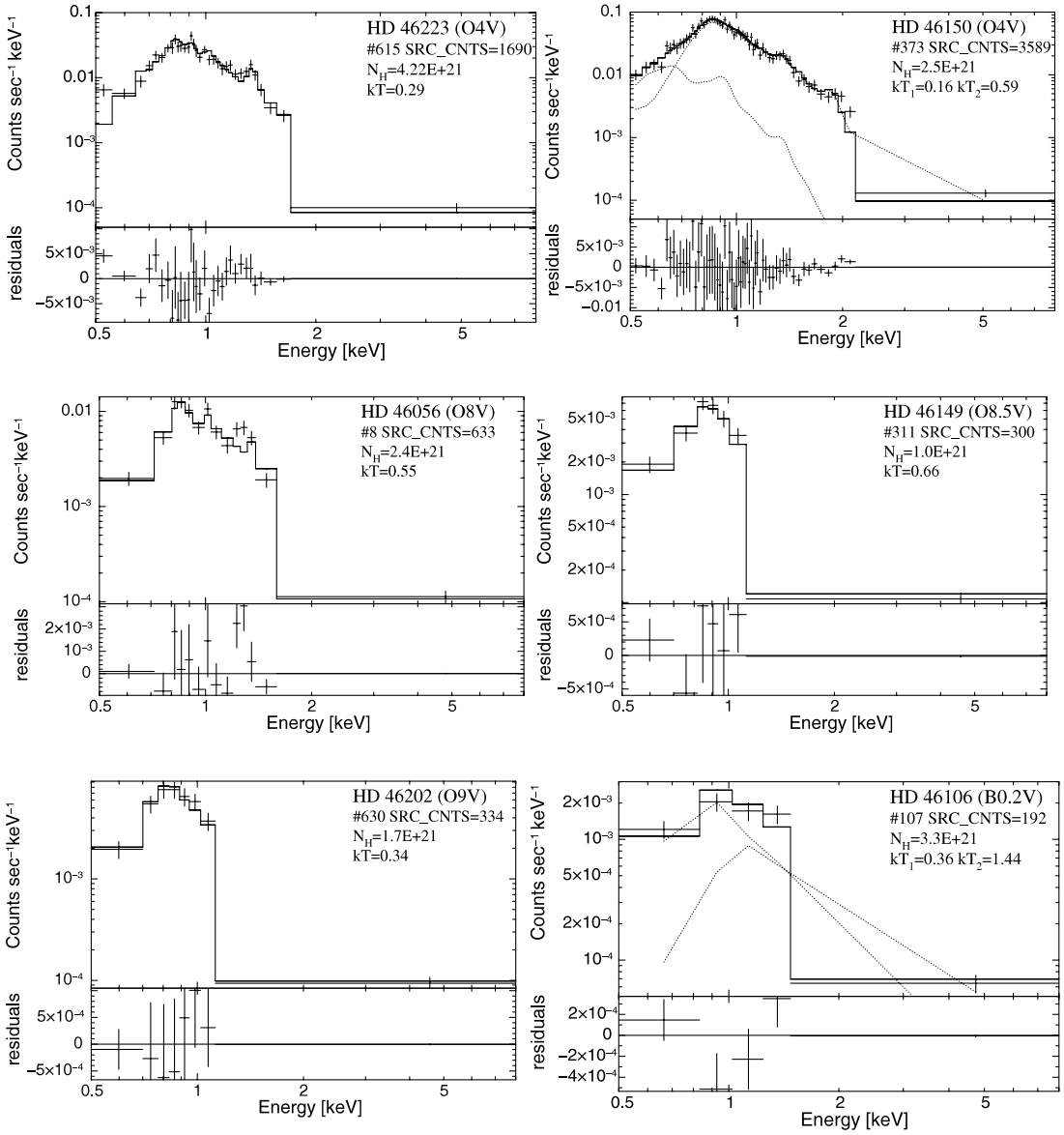

FIG. 17.—Spectral fits to X-ray spectra of six O and early B stars. Source name, source counts, and fit parameters are marked in each panel. The two model components are shown as the dotted lines for spectra that are best fitted with two-temperature thermal plasma models.

(Berghöfer & Schmitt 1994; Berghöfer et al. 1997; Stelzer et al. 2003, 2006a). However, X-ray detections of PMS intermediate-mass stars known as HAeBe stars are widely reported (e.g., Zinnecker & Preibisch 1994; Damiani et al. 1994; Berghöfer et al. 1996; Stelzer et al. 2005; Hamaguchi et al. 2005). A systematic *Chandra* archival study (Stelzer et al. 2006b) rules out radiative winds as the origin for X-ray emission in HAeBe stars based on the observed high X-ray temperatures. Thus, an X-ray–generating mechanism from magnetic flares similar to late-type stars or emission from an unknown/unresolved companion is favored, although the role of accretion for the production of X-rays remains unclear (Hamaguchi et al. 2005; Stelzer et al. 2006b).

Using masses estimated from the NIR CMD (Fig. 6), we detect around 50 stars in the intermediate-mass range $2\ M_{\odot} \lesssim M \lesssim 8\ M_{\odot}$. The absorption-corrected X-ray luminosities of the detected sources in the 0.5–8.0 keV band are in the range of $\log L_{t,c} \sim 29.5$–31.8 ergs s^{-1}. This is fully consistent with the level of X-ray emission detected in HAeBe stars from Hamaguchi et al. (2005) and Stelzer et al. (2006b), but also with the level expected from late-type companions. Optical spectral classification of these stars may further clarify the link between the X-ray emission properties and the spectral types (e.g., Li et al. 2002). Eight of these stars show significant temporal variability ($P_{\text{K-S}} \leq 0.005$), which strongly supports emission from flaring, possibly from unresolved low-mass companions. For example, source 804 shows a big flare during our long observation (Fig. 4). The rising and decay times during the flare are rather symmetric. The count rate during the peak of the flare is 18 times higher than that of the quiescent level. As noted in § 3.1, source 44 is a previously identified Herbig Be star in NGC 2244 (Li et al. 2002). We detected 40 net counts at its optical position in 94 ks. The fit to its X-ray spectrum indicates a low absorption and a hard ($kT = 2.8$ keV) plasma with a nonvariable light curve.

5.3. *X-Rays from Other Interesting Sources*

Herbig-Haro jets and knots.—Two optical jet systems, namely, Rosette HH 1 (R.A. = 06$^{\text{h}}$32$^{\text{m}}$20.76$^{\text{s}}$, decl. = 04°53′02.9″) and HH 2 (R.A. = 06$^{\text{h}}$32$^{\text{m}}$14.14$^{\text{s}}$, decl. = 05°02′17.95″ [J2000.0]), have been discovered in the Rosette Nebula (Li 2003, 2005; Li & Rector 2004; Meaburn et al. 2005; Li et al. 2007). HH 1 consists of

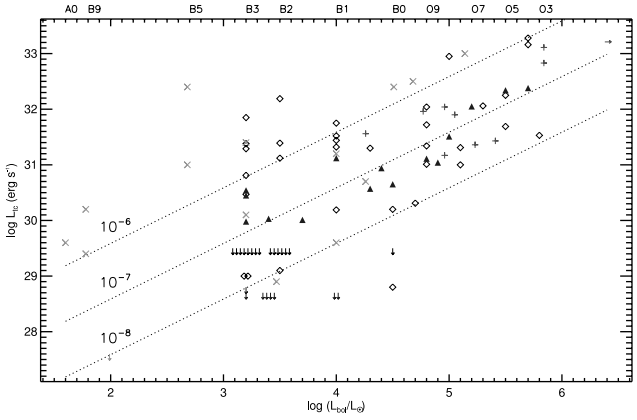

FIG. 18.—L_X vs. L_{bol} relation for X-ray–detected O and early B stars. The samples are from the NGC 2244 cluster (*filled triangles*; this work, Table 7), the ONC (*crosses*; Stelzer et al. 2005), and the massive star-forming regions M17 (*diamonds*; Broos et al. 2007) and NGC 6357 (*plus signs*; Wang et al. 2007). Upper limits are marked as arrows. The bolometric luminosities are adopted from Broos et al. (2007) to be consistent. [*See the electronic edition of the Journal for a color version of this figure*.]

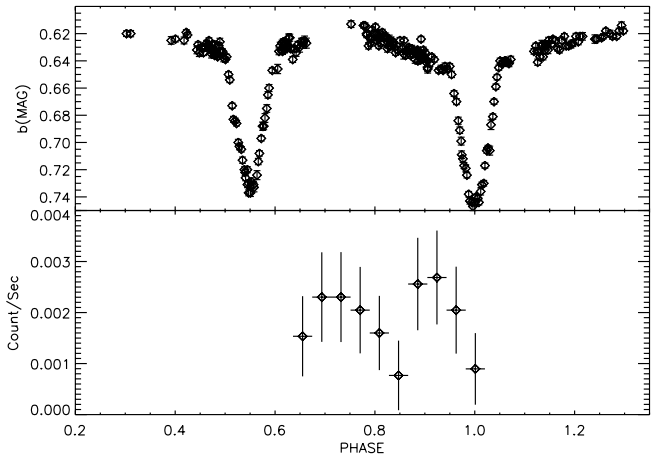

FIG. 19.—X-ray light curve of the eclipsing binary V578 Mon (*bottom*), together with the optical light curve (*b*-band photometry with 1 σ error bars taken from Hensberge et al. 2000) in orbital phases (*top*). The orbital phase is calculated using the eclipse ephemeris reported in Hensberge et al. (2000).

a collimated jet originating from a faint optical star with a mass-loss rate $\dot{M} \sim 10^{-8}\ M_\odot$. We have detected X-ray emission (ACIS source 743) coincident with the location of the exciting source of HH 1, a weak-lined T Tauri star (F8 Ve; Li 2005). At the location of the base, knot, or terminal shock of the jet, the distribution of X-ray photons is consistent with background counts. No concentration of photons is coincident with the shock structure seen in optical near the end of the collimated jet. The X-ray spectrum of the star is soft, with $kT \sim 0.8$ keV and a negligible absorption column. It has been suggested that the combination of low extinction and high Lyman photon flux inside the Rosette Nebula makes the jet optically visible (Meaburn et al. 2005).

A group of bright ionized knots in the Rosette Nebula were proposed to be collisionally ionized, either by bow shocks formed around globules by the strong winds from O stars, which are then overrun by an expanding shell, or by collimated flows of shocked gas driven by the wind (Meaburn & Walsh 1986). Chen et al. (2004) found an X-ray source in the nebulous region D with high-speed knots and identified two stars as counterparts within *ROSAT* positional errors. We examined our *Chandra* image with much higher resolution at all knot locations. No X-ray emission was found to be associated with these high-speed knots, but we detected point sources coincident with optical stars embedded in the nebulous region. ACIS source 678 (source 30 in Chen et al. 2004) matches the position of HD 259210, a likely foreground star with spectral type A1 V.

Binaries.—The eclipsing binary V578 Mon, used to determine the age and distance to NGC 2244, is detected in our X-ray image with 186 net counts (source 476). It consists of two early B-type stars, one of the very few massive eclipsing systems known (Harries & Hilditch 1998). Its orbital period is precisely determined in the optical to be $P = 2.40848 \pm 0.00001$ days (Hensberge et al. 2000). Using the eclipse ephemeris and the date at the beginning of our observation, we examined the X-ray light curve together with the optical light curve with orbital phases (Fig. 19). No significant variability is suggested by a K-S test for the X-ray light curve, although dips might be seen in the X-ray light curve around phase $\phi = 0.85$ and 1.0, where the primary eclipse is expected. This could be one of the rare cases where X-ray eclipses can be used to constrain emitting geometry (e.g., Schmitt & Favata 1999). However, this could simply be a statistical fluctuation given the limited number of counts. The spectral fit gives a plasma temperature of $kT \sim 1.6$ keV with low absorption, $\log N_H = 20.6\ \mathrm{cm}^{-2}$.

Park & Sung (2002) noted a suspected PMS binary system ([PS02] 125 and [PS02] 126). An optical spectrum of the unresolved binary shows Hα in emission and Li I λ6708 in absorption (Chen et al. 2004), confirming its youth. We resolve the system as a close pair of ACIS sources (243 and 242). Their spectral fits give a rather hard $kT \sim 2.9$ keV for source 243 and $kT \sim 1.5$ keV for source 242; they share the same $\log N_H = 21.4\ \mathrm{cm}^{-2}$. The light curve of source 242 is constant, while source 243 shows possible but not significant variation ($P_{K\text{-}S} = 0.03$).

Magnetic star.—Bagnulo et al. (2004) discovered an extraordinarily strong magnetic field in the very young cluster member NGC 2244-334 (=[OI81] 334; spectral type B3; R.A. = $06^h32^m51.79^s$, decl. = $+04^\circ47'16.1''$ [J2000.0]), ranking as the second strongest longitudinal field known among nondegenerate stars (after HD 215441, or Babcock's star; Borra & Landstreet 1978). We detected a 10 count X-ray source (source 899, CXOU J063251.79+044715.9) at its position in the 20 ks observation (it was not covered by the deep observation).

Elephant trunks.—Schneps et al. (1980) identified several spectacular elephant trunk globules in the northwest part of the Rosette Nebula. Only one of them, a small isolated globule denoted R1, is in our FOV. One X-ray source (169), probably by chance superposition, is located 6″ away from the bright rim of this dark globule. No other X-ray/IR source can be found inside the globule.

In the southeast quadrant of the nebula toward the RMC, another molecular pillar is prominent. This region is also highlighted in a recent *Spitzer* survey (Balog et al. 2007), as the size of the pillar is comparable to the largest "pillar of creation" in M16. Chen et al. (2004) noted shocked gas near the pillar, perhaps due to strong winds from a star nearby that was matched to one of the *ROSAT* sources. In the vicinity of this pillar, a luminous X-ray source (source 919, CXOU J063309.61+044624.3) is detected in our observation, but it is not located at the tip of the elephant trunk (see Fig. 20). Its X-ray spectrum can be fitted well with $\log N_H = 21.2\ \mathrm{cm}^{-2}$ and a hard ($kT = 3.3$ keV) plasma. With an unusually high luminosity of $\log L_{t,c} \sim 32.2\ \mathrm{ergs\ s}^{-1}$, it is comparable to the earliest O stars. The light curve is variable, as shown in Figure 4. The count rate doubles after the first 6 ks and remains in a high state for ~13 ks. Its IR counterpart is also bright, with a *K*-band magnitude of 9.6 mag that is similar to the observed B0–B2 stars in the field. Its location in the CMD also suggests a spectral type of B0–B1. No *K* excess is seen. As an early B-type star, its X-ray variability can be explained by an unresolved late-type

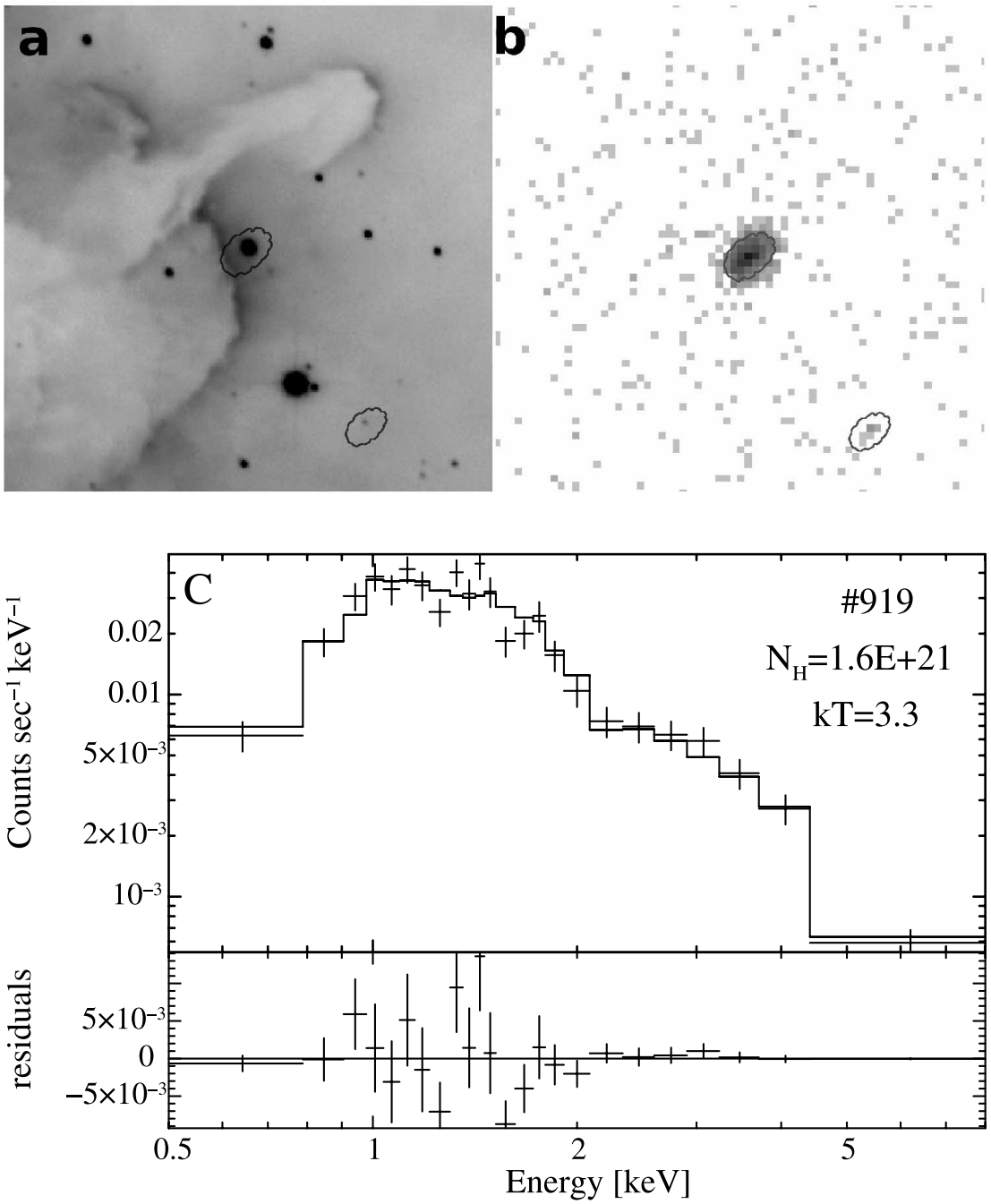

FIG. 20.—(*a*) Hα image of the neighborhood of ACIS source 919, near a molecular pillar. (*b*) X-ray image of the same region. The $2.5' \times 2.5'$ images are both centered at the X-ray–bright star 919. (*c*) Spectral fit to the X-ray spectrum of source 919 with $\log N_{\rm H} = 21.2$ and a hard ($kT = 3.3$ keV) plasma.

companion, although the light curve does not follow the typical PMS fast-rise and slow-decay phase. A similar transition between high and low states seen in θ^2 Ori A is investigated by Schulz et al. (2006) and interpreted as possibly the reconnection from magnetic interactions in a close binary system.

6. SUMMARY

We present a high spatial resolution X-ray study of the NGC 2244 cluster in the Rosette Nebula obtained via deep *Chandra* observations. Our main findings follow:

1. We detect 919 X-ray sources with a limiting X-ray sensitivity of $L_{t,c} \sim 1 \times 10^{29}$ ergs s^{-1}. Positional coincidence matching yields a total of 712 ONIR counterparts. We estimate 8% extragalactic and Galactic contamination. The rest of the X-ray sources without ONIR counterparts are likely new NGC 2244 members clustered around the massive star HD 46150 or deeply embedded in the cloud. The X-ray–detected population provides the first deep probe of the rich low-mass population in this massive cluster.

2. The locations of most ACIS sources in the color-magnitude plot indicate a large population of 2 Myr old PMS low-mass stars ($M \lesssim 2\,M_\odot$) subject to a visual extinction of $1 \lesssim A_V \lesssim 2$ at 1.4 kpc. We derive an overall K excess disk frequency of $\sim$6% for stars with mass $M \gtrsim 0.5\,M_\odot$ using the X-ray–selected sample, slightly lower than the 10% K excess disk fraction using a FLAMINGOS-selected sample. Both fractions are significantly lower than the 45% mid-IR disk fraction in a *Spitzer* sample that is more sensitive to disks. We emphasize that the combination of

young stars identified in X-rays (mostly Class III stars) and those selected through IR colors will provide the best census to date for the young stellar population of this region. Three objects have Class I colors.

3. The derived XLF ($L_{h,c}$) for NGC 2244 is compared to the XLFs of the ONC, M17, Cep B, and NGC 6357; this exercise indicates that the unobscured population in NGC 2244 is 1.2 times larger than that of the ONC, or ~1000 stars detectable in COUP-sensitivity X-ray observations. Taking into account the obscured population, the total stellar population in NGC 2244 is ~2000, in good agreement with the estimated population from the spatially complete 2MASS study. The XLF and KLF suggest a normal Salpeter IMF for NGC 2244; we do not confirm a top-heavy IMF reported from earlier optical studies.

4. We examine the spatial distribution of the X-ray–identified NGC 2244 cluster members; the stellar surface density map suggests a spherical cluster with substructure. We confirm the existence of a subcluster around HD 46150 with ~50 members in a 1 pc region; a second small subcluster consisting of a number of late-type stars is also found. The O4 star HD 46223 has few companions. The radial density profile of NGC 2244 shows a larger relaxed structure around the central subcluster. Similar structure is seen in NGC 6357. No evidence for significant mass segregation is found in this cluster. Altogether we suggest that this 2 Myr cluster is not dynamically evolved and has a complex star formation history. Our results will strongly constrain models of the cluster formation process.

5. We detected all nine OB stars with spectral types B0.5 or earlier, but only 6 out of 14 B stars with spectral types B1–B3 in our FOV. X-ray spectra for the massive stars in NGC 2244 all show soft emission. We confirm the long-standing $\log(L_X/L_{bol}) \sim -7$ relation for the NGC 2244 O stars. Large scatter around this correlation was found for the B stars.

6. We report X-ray emission detected from a few interesting individual objects, including the ionizing source of the optical jet Rosette HH 1, binary systems, a magnetic star, and a possible X-ray–luminous uncataloged massive star.

We thank the referee, Scott Wolk, for his time and for many useful comments that improved this work. We thank Ed Churchwell and Steinn Sigurdsson for helpful discussions on the cluster structure and dynamics. We thank Travis Rector and Mark Heyer for kindly providing the KPNO MOSAIC images of the Rosette Nebula and the CO emission maps of the Rosette complex, respectively. This work was supported by *Chandra X-Ray Observatory* grants GO1-2008X, GO3-4010X, and GO6-7006X. FLAMINGOS was designed and constructed by the IR instrumentation group (PI: R. Elston) at the University of Florida, Department of Astronomy with support from NSF grant AST 97-31180 and Kitt Peak National Observatory. The data were collected under the NOAO Survey Program, "Towards a Complete Near-Infrared Spectroscopic Survey of Giant Molecular Clouds" (PI: E. Lada), and supported by NSF grants AST 97-3367 and AST 02-02976 to the University of Florida. E. A. L. also acknowledges support from NASA LTSA NNG05D66G. This publication makes use of data products from the Two Micron All Sky Survey, which is a joint project of the University of Massachusetts and the Infrared Processing and Analysis Center/California Institute of Technology, funded by NASA and the National Science Foundation. This research has made use of the SIMBAD database and the VizieR catalog access tool, operated at CDS, Strasbourg, France.

Facilities: CXO (ACIS)

REFERENCES

Adams, J. D., Stauffer, J. R., Monet, D. G., Skrutskie, M. F., & Beichman, C. A. 2001, AJ, 121, 2053
Albacete Colombo, J. F., Flaccomio, E., Micela, G., Sciortino, S., & Damiani, F. 2007, A&A, 464, 211
Arnaud, K. A. 1996, in ASP Conf. Ser. 101, Astronomical Data Analysis Software and Systems V, ed. G. H. Jacoby & J. Barnes (San Francisco: ASP), 17
Babel, J., & Montmerle, T. 1997a, A&A, 323, 121
———. 1997b, ApJ, 485, L29
Bagnulo, S., Hensberge, H., Landstreet, J. D., Szeifert, T., & Wade, G. A. 2004, A&A, 416, 1149
Balog, Z., Muzerolle, J., Rieke, G. H., Su, K. Y. L., & Young, E. T. 2007, ApJ, 660, 1532
Balog, Z., Rieke, G. H., Su, K. Y. L., Muzerolle, J., & Young, E. T. 2006, ApJ, 650, L83
Berghöfer, T. W., & Christian, D. J. 2002, A&A, 384, 890
Berghöfer, T. W., & Schmitt, J. H. M. M. 1994, A&A, 292, L5
Berghöfer, T. W., Schmitt, J. H. M. M., & Cassinelli, J. P. 1996, A&AS, 118, 481
Berghöfer, T. W., Schmitt, J. H. M. M., Danner, R., & Cassinelli, J. P. 1997, A&A, 322, 167
Bessell, M. S., & Brett, J. M. 1988, PASP, 100, 1134
Binney, J., & Tremaine, S. 1987, Galactic Dynamics (Princeton: Princeton Univ. Press)
Blitz, L., & Thaddeus, P. 1980, ApJ, 241, 676
Bonatto, C., Santos, J. F. C., Jr., & Bica, E. 2006, A&A, 445, 567
Bonnell, I. A., & Davies, M. B. 1998, MNRAS, 295, 691
Borra, E. F., & Landstreet, J. D. 1978, ApJ, 222, 226
Brandt, W. N., et al. 2001, AJ, 122, 2810
Broos, P. S., Feigelson, E. D., Townsley, L. K., Getman, K. V., Wang, J. F., Garmire, G. P., Jiang, Z., & Tsuboi, Y. 2007, ApJS, 169, 353
Broos, P. S., Townsley, L. K., Getman, K. V., & Bauer, F. E. 2002, ACIS Extract, An ACIS Point Source Extraction Package (University Park: Pennsylvania State Univ.)
Burningham, B., Naylor, T., Littlefair, S. P., & Jeffries, R. D. 2005, MNRAS, 363, 1389
Carpenter, J. M., Meyer, M. R., Dougados, C., Strom, S. E., & Hillenbrand, L. A. 1997, AJ, 114, 198
Cash, W. 1979, ApJ, 228, 939
Celnik, W. E. 1985, A&A, 144, 171
———. 1986, A&A, 160, 287
Chen, L., de Grijs, R., & Zhao, J. L. 2007, AJ, 134, 1368
Chen, W. P., Chiang, P. S., & Li, J. Z. 2004, Chinese J. Astron. Astrophys., 4, 153
Chini, R., Hoffmeister, V., Kimeswenger, S., Nielbock, M., Nürnberger, D., Schmidtobreick, L., & Sterzik, M. 2004, Nature, 429, 155
Chini, R., Hoffmeister, V. H., Nielbock, M., Scheyda, C. M., Nürnberger, D., Feigelson, E. D., Getman, K., & Townsley, L. K. 2005, in IAU Symp. 227, Massive Star Birth: A Crossroads of Astrophysics, ed. R. Cesaroni et al. (Cambridge: Cambridge Univ. Press), 145
Chlebowski, T., Harnden, F. R., & Sciortino, S. 1989, ApJ, 341, 427
Clarke, C. J., Bonnell, I. A., & Hillenbrand, L. A. 2000, in Protostars and Planets IV, ed. V. Mannings, A. P. Boss, & S. S. Russell (Tucson: Univ. Arizona Press), 151
Comeron, F., & Pasquali, A. 2007, A&A, 467, L23
Corcoran, M. F., et al. 1994, ApJ, 436, L95
Cox, P., Deharveng, L., & Leene, A. 1990, A&A, 230, 181
Cutri, R. M., et al. 2003, The IRSA 2MASS All-Sky Point Source Catalog, NASA/IPAC Infrared Science Archive
Damiani, F., Micela, G., Sciortino, S., & Harnden, F. R., Jr. 1994, ApJ, 436, 807
de Jager, C., & Nieuwenhuijzen, H. 1987, A&A, 177, 217
Dias, W. S., Assafin, M., Flório, V., Alessi, B. S., & Líbero, V. 2006, A&A, 446, 949
Dickey, J. M., & Lockman, F. J. 1990, ARA&A, 28, 215
Ebeling, H., White, D. A., & Rangarajan, F. V. N. 2006, MNRAS, 368, 65
Elston, R., Raines, S. N., Hanna, K. T., Hon, D. B., Julian, J., Horrobin, M., Harmer, C. F. W., & Epps, H. W. 2003, Proc. SPIE, 4841, 1611

Evans, N. R., Schlegel, E. M., Waldron, W. L., Seward, F. D., Krauss, M. I., Nichols, J., & Wolk, S. J. 2004, ApJ, 612, 1065
Ezoe, Y., Kokubun, M., Makishima, K., Sekimoto, Y., & Matsuzaki, K. 2006, ApJ, 638, 860
Favata, F., Flaccomio, E., Reale, F., Micela, G., Sciortino, S., Shang, H., Stassun, K. G., & Feigelson, E. D. 2005, ApJS, 160, 469
Favata, F., & Micela, G. 2003, Space Sci. Rev., 108, 577
Feigelson, E., Townsley, L., Güdel, M., & Stassun, K. 2007, in Protostars & Planets V, ed. B. Reipurth, D. Jewitt, & K. Keil (Tucson: Univ. Arizona Press), 313
Feigelson, E. D., Broos, P., Gaffney, J. A., III, Garmire, G., Hillenbrand, L. A., Pravdo, S. H., Townsley, L., & Tsuboi, Y. 2002, ApJ, 574, 258
Feigelson, E. D., & Montmerle, T. 1999, ARA&A, 37, 363
Feigelson, E. D., et al. 2005, ApJS, 160, 379
Freeman, P. E., Kashyap, V., Rosner, R., & Lamb, D. Q. 2002, ApJS, 138, 185
Froebrich, D., Scholz, A., Eislöffel, J., & Murphy, G. C. 2005, A&A, 432, 575
Gagné, M., Oksala, M. E., Cohen, D. H., Tonnesen, S. K., ud-Doula, A., Owocki, S. P., Townsend, R. H. D., & MacFarlane, J. J. 2005, ApJ, 628, 986
Getman, K. V., Feigelson, E. D., Garmire, G., Broos, P., & Wang, J. 2007, ApJ, 654, 316
Getman, K. V., Feigelson, E. D., Grosso, N., McCaughrean, M. J., Micela, G., Broos, P., Garmire, G., & Townsley, L. 2005a, ApJS, 160, 353
Getman, K. V., et al. 2005b, ApJS, 160, 319
———. 2006, ApJS, 163, 306
Gregorio-Hetem, J., Montmerle, T., Casanova, S., & Feigelson, E. D. 1998, A&A, 331, 193
Grosso, N., Montmerle, T., Feigelson, E. D., & Forbes, T. G. 2004, A&A, 419, 653
Guarcello, M. G., Prisinzano, L., Micela, G., Damiani, F., Peres, G., & Sciortino, S. 2007, A&A, 462, 245
Güdel, M., Guinan, E. F., & Skinner, S. L. 1998, in ASP Conf. Ser. 154, Cool Stars, Stellar Systems, and the Sun, ed. R. A. Donahue & J. A. Bookbinder (San Francisco: ASP), 1041
Haisch, K. E., Jr., Lada, E. A., & Lada, C. J. 2001a, AJ, 121, 2065
Haisch, K. E., Jr., Lada, E. A., Piña, R. K., Telesco, C. M., & Lada, C. J. 2001b, AJ, 121, 1512
Hamaguchi, K., Yamauchi, S., & Koyama, K. 2005, ApJ, 618, 360
Harnden, F. R., Jr., et al. 1979, ApJ, 234, L51
Harries, T. J., & Hilditch, R. W. 1998, in ASP Conf. Ser. 131, Properties of Hot Luminous Stars, ed. I. Howarth (San Francisco: ASP), 401
Hartmann, L., & Burkert, A. 2007, ApJ, 654, 988
Hensberge, H., Pavlovski, K., & Verschueren, W. 2000, A&A, 358, 553
Heyer, M. H., Williams, J. P., & Brunt, C. M. 2006, ApJ, 643, 956
Hillenbrand, L. A., & Hartmann, L. W. 1998, ApJ, 492, 540
Hillenbrand, L. A., Massey, P., Strom, S. E., & Merrill, K. M. 1993, AJ, 106, 1906
Hollenbach, D. J., Yorke, H. W., & Johnstone, D. 2000, in Protostars and Planets IV, ed. V. Mannings, A. P. Boss, & S. S. Russell (Tucson: Univ. Arizona Press), 401
Hünsch, M., Schmitt, J. H. M. M., Sterzik, M. F., & Voges, W. 1999, A&AS, 135, 319
Imanishi, K., Koyama, K., & Tsuboi, Y. 2001, ApJ, 557, 747
Isobe, T., Feigelson, E. D., & Nelson, P. I. 1986, ApJ, 306, 490
Jiang, Z., et al. 2002, ApJ, 577, 245
Johnstone, D., Hollenbach, D., & Bally, J. 1998, ApJ, 499, 758
Kenyon, S. J., Calvet, N., & Hartmann, L. 1993, ApJ, 414, 676
Kharchenko, N. V., Piskunov, A. E., Röser, S., Schilbach, E., & Scholz, R.-D. 2005, A&A, 438, 1163
King, I. 1962, AJ, 67, 471
Kouwenhoven, M. B. N., Brown, A. G. A., & Kaper, L. 2007, A&A, 464, 581
Kroupa, P. 2002, Science, 295, 82
———. 2004, NewA Rev., 48, 47
Lada, C. J. 1991, in NATO ASIC Proc. 342, The Physics of Star Formation and Early Stellar Evolution, ed. C. J. Lada & N. D. Kylafis (Dordrecht: Kluwer), 329
Lada, C. J., & Adams, F. C. 1992, ApJ, 393, 278
Lada, C. J., & Lada, E. A. 2003, ARA&A, 41, 57
Lada, C. J., Muench, A. A., Haisch, K. E., Jr., Lada, E. A., Alves, J. F., Tollestrup, E. V., & Willner, S. P. 2000, AJ, 120, 3162
Lada, C. J., Muench, A. A., Lada, E. A., & Alves, J. F. 2004, AJ, 128, 1254
Lada, C. J., et al. 2006, AJ, 131, 1574
Lada, E. A. 1992, ApJ, 393, L25
Lada, E. A., & Lada, C. J. 1995, AJ, 109, 1682
Leahy, D. A. 1985, MNRAS, 217, 69
Li, J. Z. 2003, Chinese J. Astron. Astrophys., 3, 495
———. 2005, ApJ, 625, 242
Li, J. Z., Chu, Y. H., Gruendl, R. A., Bally, J., & Su, W. 2007, ApJ, 659, 1373
Li, J. Z., & Rector, T. A. 2004, ApJ, 600, L67
Li, J. Z., & Smith, M. 2005a, AJ, 130, 721
Li, J. Z., & Smith, M. D. 2005b, ApJ, 620, 816
Li, J. Z., Wu, C. H., Chen, W. P., Rector, T., Chu, Y. H., & Ip, W. H. 2002, AJ, 123, 2590
Linsky, J. L., Gagné, M., Mytyk, A., McCaughrean, M., & Andersen, M. 2007, ApJ, 654, 347
Lucy, L. B. 1974, AJ, 79, 745
Lucy, L. B., & White, R. L. 1980, ApJ, 241, 300
Marschall, L. A., van Altena, W. F., & Chiu, L.-T. G. 1982, AJ, 87, 1497
Martins, F., Schaerer, D., & Hillier, D. J. 2005, SF2A-2005: Semaine de l'Astrophysique Francaise, ed. F. Casoli et al. (Les Ulis Cedex A: EDP Sciences), 633
Massey, P., Johnson, K. E., & Degioia-Eastwood, K. 1995, ApJ, 454, 151
McMillan, S. L. W., Vesperini, E., & Portegies Zwart, S. F. 2007, ApJ, 655, L45
Meaburn, J., López, J. A., Richer, M. G., Riesgo, H., & Dyson, J. E. 2005, AJ, 130, 730
Meaburn, J., & Walsh, J. R. 1986, MNRAS, 220, 745
Meyer, M. R., Calvet, N., & Hillenbrand, L. A. 1997, AJ, 114, 288
Monet, D. G., et al. 2003, AJ, 125, 984
Moretti, A., Campana, S., Lazzati, D., & Tagliaferri, G. 2003, ApJ, 588, 696
Mori, K., Tsunemi, H., Miyata, E., Baluta, C. J., Burrows, D. N., Garmire, G. P., & Chartas, G. 2001, in ASP Conf. Ser. 251, New Century of X-Ray Astronomy, ed. H. Inoue & H. Kunieda (San Francisco: ASP), 576
Muench, A. A., Lada, C. J., Luhman, K. L., Muzerolle, J., & Young, E. 2007, AJ, 134, 411
Muench, A. A., Lada, E. A., Lada, C. J., & Alves, J. 2002, ApJ, 573, 366
Muno, M. P., Bauer, F. E., Bandyopadhyay, R. M., & Wang, Q. D. 2006, ApJS, 165, 173
Muzerolle, J., Calvet, N., & Hartmann, L. 2001, ApJ, 550, 944
Muzerolle, J., Hartmann, L., & Calvet, N. 1998, AJ, 116, 455
Natta, A., Grinin, V., & Mannings, V. 2000, in Protostars and Planets IV, ed. V. Mannings, A. P. Boss, & S. S. Russell (Tucson: Univ. Arizona Press), 559
Nielbock, M., Chini, R., Jütte, M., & Manthey, E. 2001, A&A, 377, 273
O'Dell, C. R., & Wong, K. 1996, AJ, 111, 846
Ogura, K., & Ishida, K. 1981, PASJ, 33, 149
Owocki, S. P., Castor, J. I., & Rybicki, G. B. 1988, ApJ, 335, 914
Owocki, S. P., & Cohen, D. H. 1999, ApJ, 520, 833
Pallavicini, R., Golub, L., Rosner, R., Vaiana, G. S., Ayres, T., & Linsky, J. L. 1981, ApJ, 248, 279
Park, B.-G., & Sung, H. 2002, AJ, 123, 892
Perez, M. R. 1991, Rev. Mex. AA, 22, 99
Pflamm-Altenburg, J., & Kroupa, P. 2006, MNRAS, 373, 295
Phelps, R. L., & Lada, E. A. 1997, ApJ, 477, 176
Pizzolato, N., Maggio, A., & Sciortino, S. 2000, A&A, 361, 614
Pollock, A. M. T., Corcoran, M. F., Stevens, I. R., & Williams, P. M. 2005, ApJ, 629, 482
Preibisch, T., & Feigelson, E. D. 2005, ApJS, 160, 390
Preibisch, T., et al. 2005, ApJS, 160, 401
Rauw, G., Nazé, Y., Gosset, E., Stevens, I. R., Blomme, R., Corcoran, M. F., Pittard, J. M., & Runacres, M. C. 2002, A&A, 395, 499
Rho, J., Ramírez, S. V., Corcoran, M. F., Hamaguchi, K., & Lefloch, B. 2004, ApJ, 607, 904
Robin, A. C., Reylé, C., Derrière, S., & Picaud, S. 2003, A&A, 409, 523
Roeser, S., & Bastian, U. 1988, A&AS, 74, 449
Román-Zúñiga, C., & Lada, E. 2008, in ASP Conf. Ser., Handbook of Star Forming Regions, in press
Román-Zúñiga, C., Elston, R., Ferreira, B., & Lada, E. 2008, ApJ, 672, 861
Román-Zúñiga, C. G. 2006, Ph.D. thesis, Univ. Florida
Román-Zúñiga, C. G., Lada, E. A., & Williams, J. P. 2005, Rev. Mex. AA Ser. Conf., 24, 66
Sana, H., Rauw, G., Nazé, Y., Gosset, E., & Vreux, J.-M. 2006, MNRAS, 372, 661
Schilbach, E., Kharchenko, N. V., Piskunov, A. E., Röser, S., & Scholz, R.-D. 2006, A&A, 456, 523
Schmitt, J. H. M. M. 1997, A&A, 318, 215
Schmitt, J. H. M. M., & Favata, F. 1999, Nature, 401, 44
Schmitt, J. H. M. M., Fleming, T. A., & Giampapa, M. S. 1995, ApJ, 450, 392
Schmitt, J. H. M. M., Golub, L., Harnden, F. R., Jr., Maxson, C. W., Rosner, R., & Vaiana, G. S. 1985, ApJ, 290, 307
Schneps, M. H., Ho, P. T. P., & Barrett, A. H. 1980, ApJ, 240, 84
Schulz, N. S., Canizares, C., Huenemoerder, D., & Tibbets, K. 2003, ApJ, 595, 365
Schulz, N. S., Testa, P., Huenemoerder, D. P., Ishibashi, K., & Canizares, C. R. 2006, ApJ, 653, 636
Sharpless, S. 1954, ApJ, 119, 334
Siess, L., Dufour, E., & Forestini, M. 2000, A&A, 358, 593
Skinner, S., Güdel, M., Schmutz, W., & Zhekov, S. 2006, Ap&SS, 304, 97

Skinner, S. L., Zhekov, S. A., Palla, F., & Barbosa, C. L. D. R. 2005, MNRAS, 361, 191
Smith, R. K., Brickhouse, N. S., Liedahl, D. A., & Raymond, J. C. 2001, ApJ, 556, L91
Stassun, K. G., van den Berg, M., Feigelson, E., & Flaccomio, E. 2006, ApJ, 649, 914
Stelzer, B., Flaccomio, E., Montmerle, T., Micela, G., Sciortino, S., Favata, F., Preibisch, T., & Feigelson, E. D. 2005, ApJS, 160, 557
Stelzer, B., Huélamo, N., Hubrig, S., Zinnecker, H., & Micela, G. 2003, A&A, 407, 1067
Stelzer, B., Huélamo, N., Micela, G., & Hubrig, S. 2006a, A&A, 452, 1001
Stelzer, B., Micela, G., Hamaguchi, K., & Schmitt, J. H. M. M. 2006b, A&A, 457, 223
Strom, K. M., Kepner, J., & Strom, S. E. 1995, ApJ, 438, 813
Telleschi, A., Güdel, M., Briggs, K. R., Audard, M., & Palla, F. 2007, A&A, 468, 425
Throop, H. B., & Bally, J. 2005, ApJ, 623, L149
Townsley, L. K., Broos, P. S., Chartas, G., Moskalenko, E., Nousek, J. A., & Pavlov, G. G. 2002, Nucl. Instrum. Methods Phys. Res. A, 486, 716
Townsley, L. K., Broos, P. S., Feigelson, E. D., Brandl, B. R., Chu, Y.-H., Garmire, G. P., & Pavlov, G. G. 2006a, AJ, 131, 2140
Townsley, L. K., Broos, P. S., Feigelson, E. D., Garmire, G. P., & Getman, K. V. 2006b, AJ, 131, 2164
Townsley, L. K., Feigelson, E. D., Montmerle, T., Broos, P. S., Chu, Y.-H., & Garmire, G. P. 2003, ApJ, 593, 874 (T03)
Tsujimoto, M., et al. 2007, ApJ, 665, 719
ud-Doula, A., & Owocki, S. P. 2002, ApJ, 576, 413
Verschueren, W. 1991, Ph.D. thesis, Vrije Univ. Brussels
Vuong, M. H., Montmerle, T., Grosso, N., Feigelson, E. D., Verstraete, L., & Ozawa, H. 2003, A&A, 408, 581
Walborn, N. R., et al. 2002, AJ, 123, 2754
Waldron, W. L., Cassinelli, J. P., Miller, N. A., MacFarlane, J. J., & Reiter, J. C. 2004, ApJ, 616, 542
Wang, J. F., Townsley, L. K., Feigelson, E. D., Getman, K. V., Broos, P. S., Garmire, G. P., & Tsujimoto, M. 2007, ApJS, 168, 100
Wang, Q. D., Dong, H., & Lang, C. 2006, MNRAS, 371, 38
Williams, J. P., & Blitz, L. 1998, ApJ, 494, 657
Williams, J. P., Blitz, L., & Stark, A. A. 1995, ApJ, 451, 252
Winston, E., et al. 2007, ApJ, 669, 493
Wolk, S. J., Spitzbart, B. D., Bourke, T. L., & Alves, J. 2006, AJ, 132, 1100
Zacharias, N., Monet, D. G., Levine, S. E., Urban, S. E., Gaume, R., & Wycoff, G. L. 2004, BAAS, 36, 1418
Zinnecker, H., & Preibisch, T. 1994, A&A, 292, 152